

Chapter 4

Results and discussion

The results of this research include were investigation and characterization of pump plunger. The purposed thermal spray materials were also characterized prior to coating fabrication. During spraying, in-flight particles and splat were collected and characterized. Plunger was also coated with various types of coating and being performed under simulated pump conditions. All result are detailed in the following sections

4.1 Characterization of pump plunger and wear test

Result of worn surface analysis and characteristics of used pump plunger include roughness, thickness, microstructure, porosity, hardness, and abrasive wear resistance.

4.1.1 Worn surface analysis of used pump plunger

There are various models of reciprocating pumps used for natural gas and crude oil. The most commonly used by this studied site is the model TXT 6121 & 6122, shown in Fig. 4.1. Three major parts of the pump include head body, plunger, and packing as detailed in Fig. 4.2.



Figure 4.1 Reciprocating pump Model TXT 6121 & 6122 size 2 3/4" [<http://www.dresser-rand.com>].

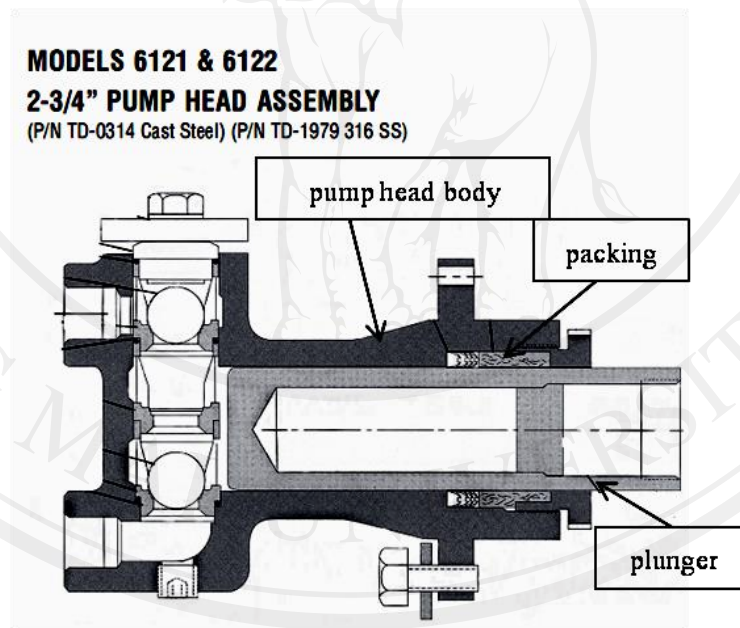


Figure 4.2 Cross-section of reciprocating pump Model TXT 6121 & 6122 size 2 3/4" [<http://www.dresser-rand.com>].

Fig. 4.3 shows wear scar of used plunger with various depth and width. Measurement of roughness across showed along the length and stroke direction. The average roughness value of $3.30 \mu\text{m}$ compared with $0.20 \mu\text{m}$ of the unworn (Table 4.1).

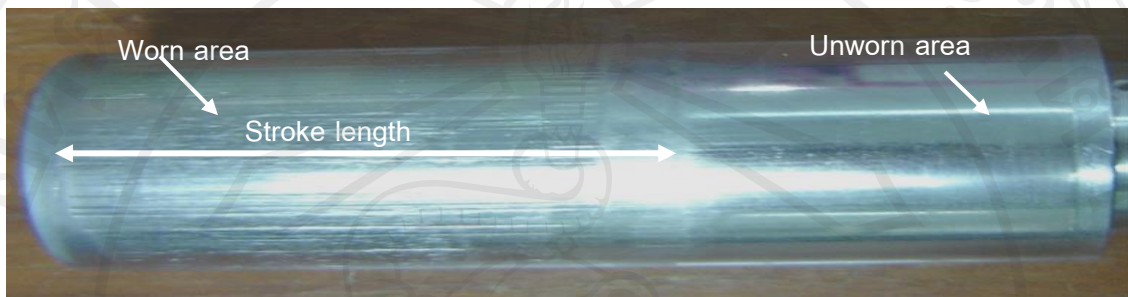


Figure 4.3 Worn and unworn areas of used plunger.

Table 4.1 Roughness of the worn area compared with the unworn area of used plunger.

| No. | Roughness (μm) | |
|----------------|-----------------------------------|-----------------------------------|
| | Worn area | Unworn area |
| 1 | 3.60 | 0.12 |
| 2 | 3.60 | 0.15 |
| 3 | 3.80 | 0.16 |
| 4 | 4.20 | 0.25 |
| 5 | 3.00 | 0.30 |
| 6 | 2.60 | 0.20 |
| 7 | 3.00 | 0.20 |
| 8 | 2.60 | 0.20 |
| 9 | 3.00 | 0.21 |
| 10 | 3.80 | 0.23 |
| Average | 3.30 ± 0.60 | 0.20 ± 0.05 |

The vernier caliper were used to measure plunger diameter of unworn and worn area. The result showed that the average diameter of unworn area was 50.82 mm while the worn area was 50.57 mm which was approximately 0.25 mm diameter decreasing as shown in Fig. 4.3.

Table 4.2 Decreasing of plunger diameter.

| No. | Diameter (mm) | | |
|----------------|--------------------|--------------------|-------------------|
| | Unworn area | Worn area | Decrease value |
| 1 | 50.81 | 50.55 | 0.26 |
| 2 | 50.84 | 50.59 | 0.25 |
| 3 | 50.82 | 50.64 | 0.18 |
| 4 | 50.82 | 50.55 | 0.27 |
| 5 | 50.82 | 50.53 | 0.29 |
| Average | 50.82 ±0.01 | 50.57 ±0.04 | 0.25 ±0.04 |

The study of reciprocating pump process showed that the plunger moving backward and was scratched. This process created pressure during sucking and pressing cycle. Although, hardness, of plunger is harder than pump seal, scratch occurred by sand particle in crude oil itself. Sand particles lead to two-body and three-body abrasion. In case of two-body abrasion, the sand particles are buried or attached to the pump seal and moving along the length of plunger. The two-body abrasion causes higher wear rate compared to the three-body abrasion surfaces. Morphological investigation of sand particles showed that the sand particles had angular morphology and sharp edge as shown in Fig. 4.4.

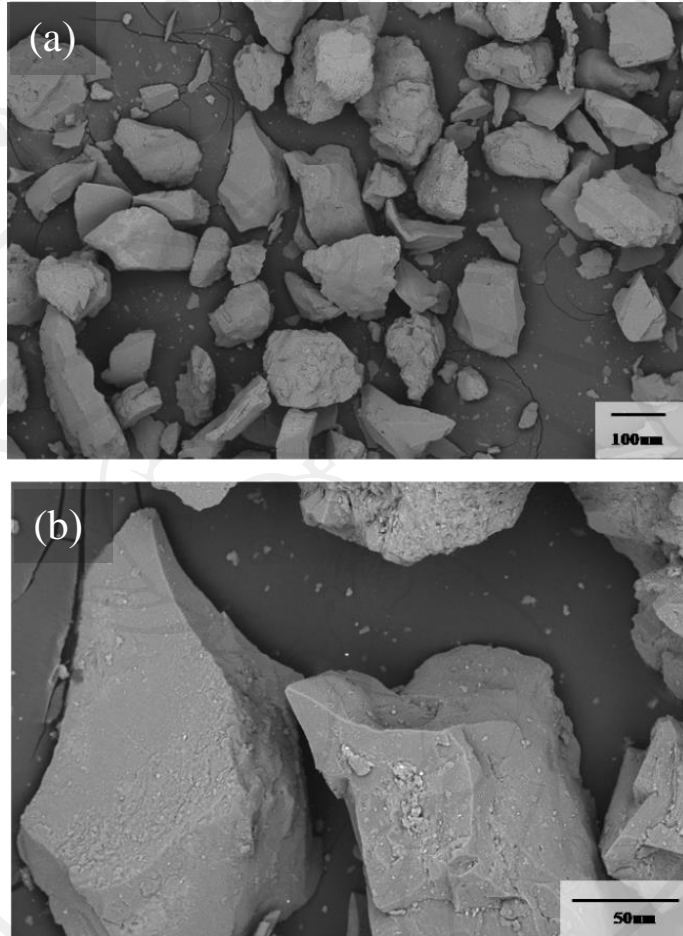


Figure 4.4 SE-SEM micrograph of sand particles in natural gas and crude oil at (a) 100X and (b) 400X magnifications.

Chemical compositions of sand particles analyzed with EDS-SEM reveals that Si and O were main composition with 34.9 and 55.7 weight percent, respectively (Table 4.3).

Fig. 4.5 shows EDS spectrum of sand particles which implied the SiO_2 as an abrasive particles.

Table 4.3 Chemical compositions of sand particles collected crude oil as analyzed by EDS-SEM.

| Element | wt% | at% |
|---------|------|------|
| Si | 34.9 | 23.4 |
| O | 55.7 | 65.4 |
| C | 6.3 | 9.7 |
| Fe | 2.3 | 0.8 |
| Al | 0.8 | 0.6 |

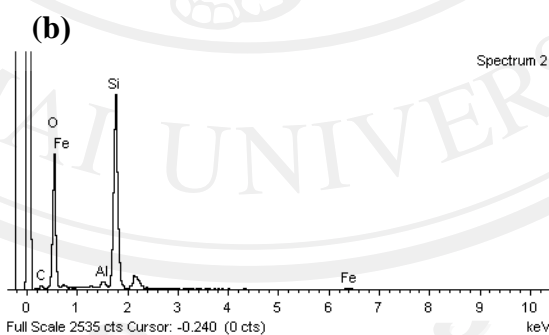
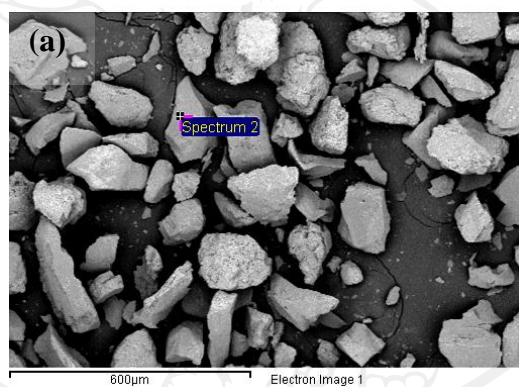


Figure 4.5 (a) SEM micrograph shows of sand particles collected from crude oil and (b) EDS spectrum of sand particle.

4.1.2 Characteristics of the original plunger

Cross-section of the plunger revealed that plunger top surface was a coating showing good adhesion between coating and the core part as shown in Fig. 4.6. It is likely that the coating was produced by spray and fuse process. [6] Details of plunger characteristic including roughness, thickness of coating, microstructure, porosity, hardness, and abrasion resistance are shown in the following sections.

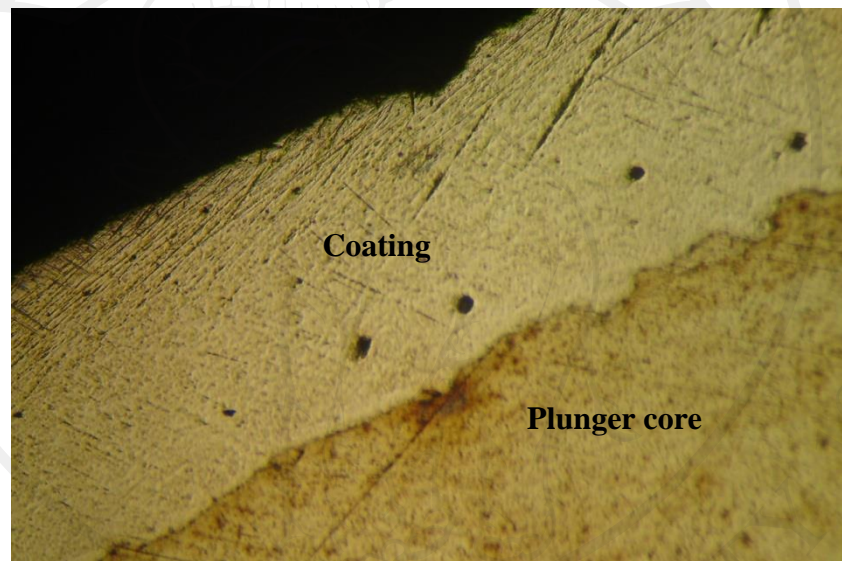


Figure 4.6 Cross-section of original plunger image at 100X magnification by optical microscope.

4.1.2.1 Roughness

The average roughness value of unworn area was the normal area was 0.20 μm Ra as shown in Table 4.1. This showed a super smooth surface roughness.

4.1.2.2 Thickness

Thickness of the unworn coating was measured by an optical microscope (OM) with the aid of SCETIS image analyzer. It was found that the average thickness value was 340 μm as shown in Table 4.4.

Table 4.4 Thickness of original plunger coating.

| No. | 1 | 2 | 3 | 4 | 5 | Average |
|-----------------------------|-----|-----|-----|-----|-----|-------------------------------|
| Thickness (μm) | 339 | 344 | 341 | 343 | 337 | 340 \pm 3 |

4.1.2.3 Microstructure

According to the SEM micrograph as shown in Fig. 4.7, it can be seen that the coating has high density and good fuse of splat, also high adhesion with substrate. Moreover, the homogeneity of phase distribution and lower porosity were contended in this coating. There are a few small pores which correspond to preparation of spray and fuse technique. [6]

Chemical compositions of the coating material and plunger core were analyzed by EDS-SEM as shown in Fig. 4.8. It was found that the coating layer has Cr, Ni, and Si as main components with 23.1, 70.3, and 6.6 (wt%), respectively. The plunger core has Cr and Fe as main components with 23.1 and 76.9 (wt%), respectively.

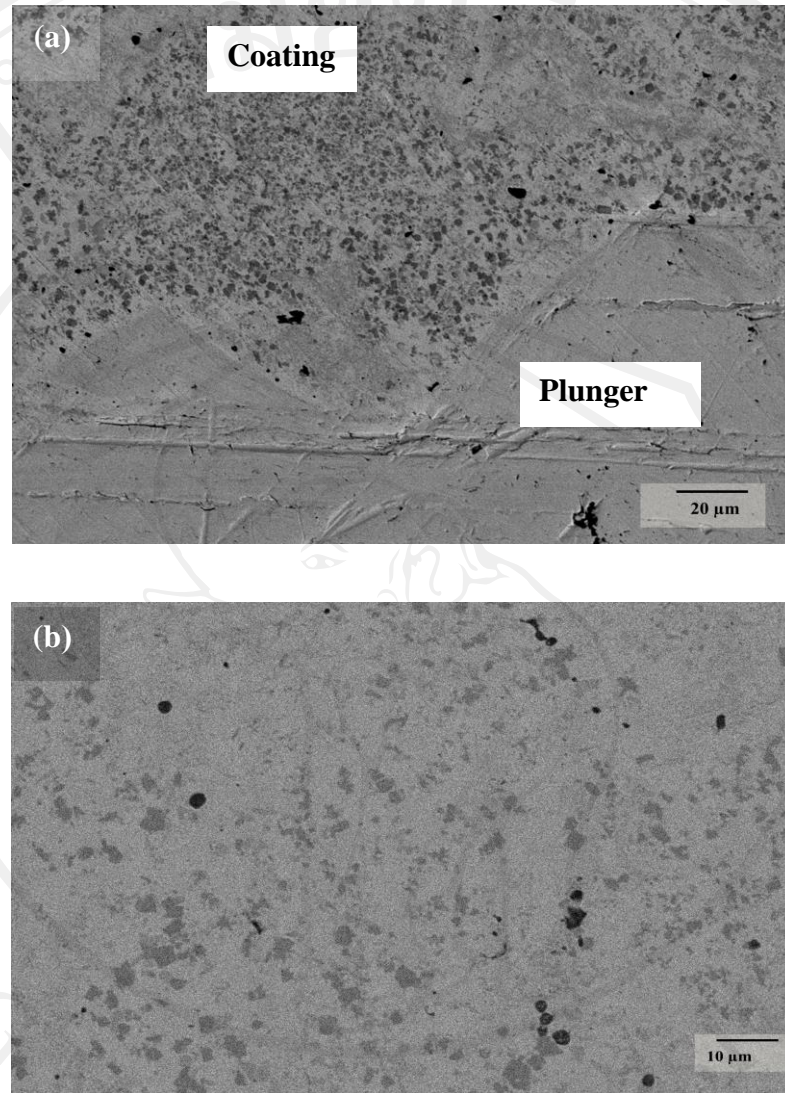


Figure 4.7 SE-SEBM micrograph showing original plunger coating and original plunger core at (a) 100X and (b) 1000X magnification.

4.1.2.4 Porosity

Porosity of the coating was analyzed by SCENTIS Image analyzer software. An average porosity is 0.70 percent, as shown in Table 4.5. This porosity rate is very low, compared to general coatings which made by spray and fuse technique.

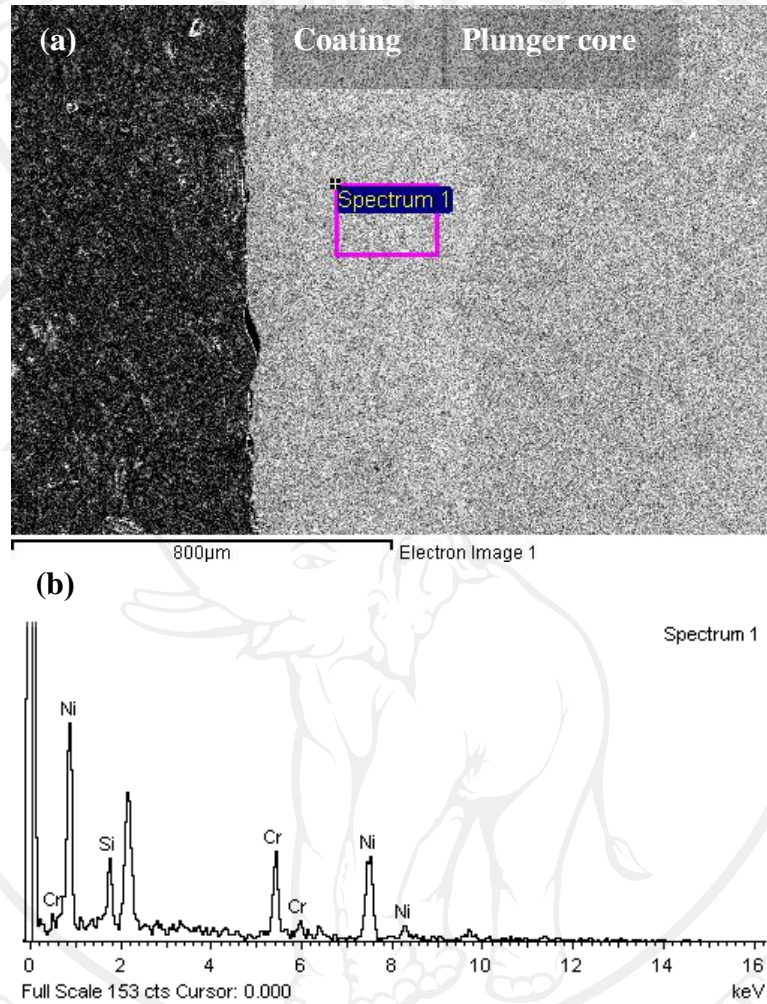


Figure 4.8 (a) BSE-SEM micrograph shows cross-section of original plunger coating and (b) EDS spectrum of original plunger coating.

Table 4.5 Porosity of original plunger coating.

| No. | 1 | 2 | 3 | 4 | 5 | 6 | 7 | 8 | 9 | 10 | Average |
|--------------|------|------|------|------|------|------|------|------|------|------|-------------------|
| Porosity (%) | 0.65 | 0.74 | 0.56 | 0.62 | 0.64 | 0.49 | 0.99 | 0.54 | 0.68 | 1.30 | 0.70 ± 0.2 |

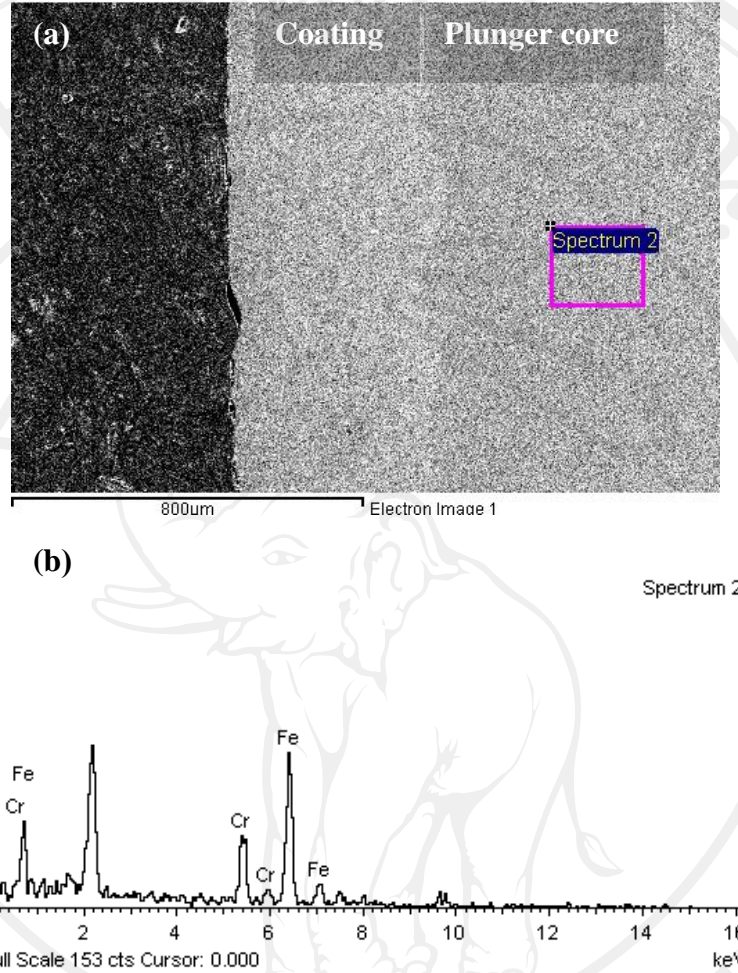


Figure 4.9 (a) BSE-SEM micrograph of cross-section original plunger core and (b) EDS spectrum of original plunger core.

4.1.2.5 Hardness

Hardness value of the coating was measured from cross-section surface of the plunger by Vickers micro hardness analyzer using the pressing weight of 300g. It was found from randomly measurement, an average hardness was 517 HV_{300g}, as shown in Table 4.6.

Table 4.6 Hardness of original plunger coating.

| No. | Hardness (HV) | No. | Hardness (HV) |
|-----|---------------|----------------|------------------|
| 1 | 445 | 9 | 457 |
| 2 | 345 | 10 | 367 |
| 3 | 455 | 11 | 456 |
| 4 | 467 | 12 | 563 |
| 5 | 657 | 13 | 670 |
| 6 | 670 | 14 | 576 |
| 7 | 556 | 15 | 650 |
| 8 | 435 | Average | 517 ± 109 |

4.1.2.6 Abrasive wear test

Wear rate of abrasive wear test of the plunger coating was measured with abrasive tester according to ASTM G65 standard, using Al₂O₃ brown alumina sand with 60 mesh size and pressing weight of 27.5 N. Data of the wear rate were collected from distance and weight loss. The wear rate could be calculated from the slope of a graph plot between distance and weight loss, as shown in Fig. 4.10. The wear rate gained was 0.045 g/m. Worn surface from the test are as shown in Fig. 4.11.

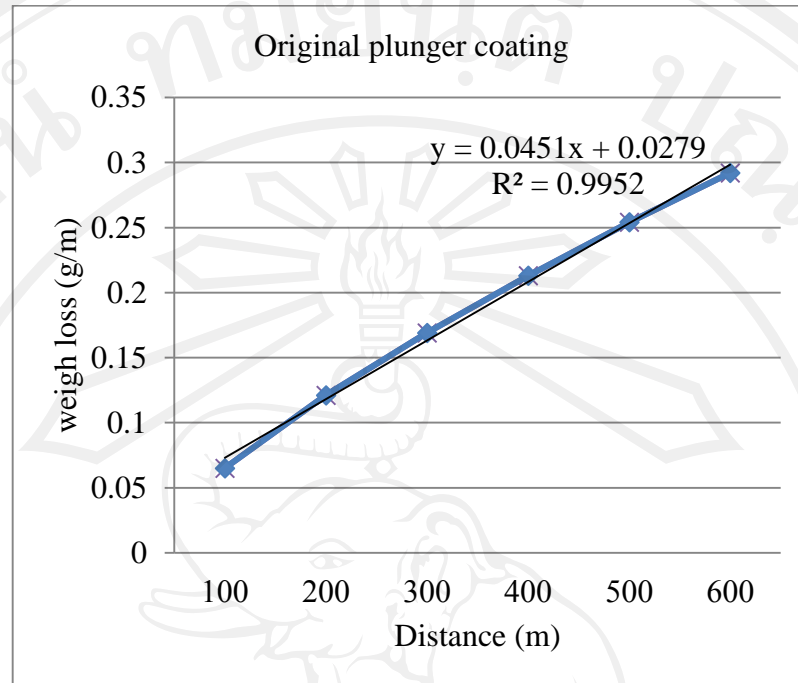


Figure 4.10 Abrasive wear of original plunger coating.

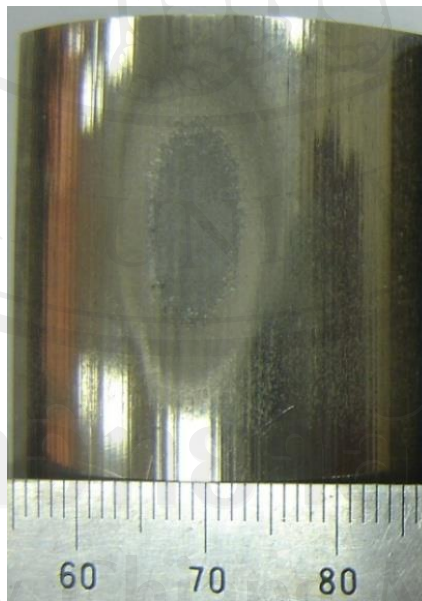


Figure 4.11 Worn surface from the abrasive test on the plunger coating.

4.2 Characteristics of starting materials

The three types of cored wires included WC-Cr-Ni, WC-Cr-Fe and W-Cr-Fe nano-composite cored wires. Characterization spray materials included size, microstructure, chemical compositions and phase compositions. Details are as follow:

Size and morphology of all cored wires cross-section by SEM. It was found that all types of cored wires consist of shell and filler inside the core as shown in Fig. 4.12.

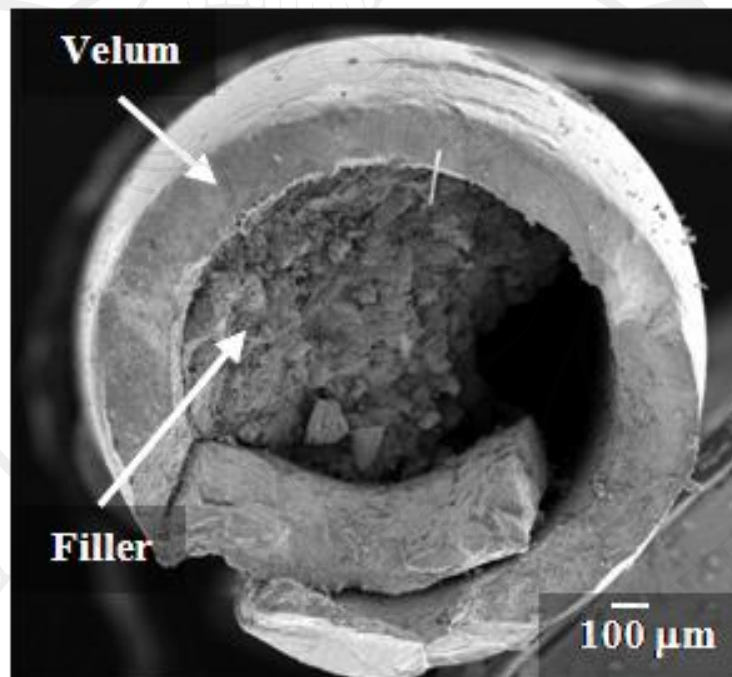


Figure 4.12 SE-SEM micrograph show example of cored wire.

4.2.1 WC-Cr-Ni cored wires

The morphology of WC-Cr-Ni cored wires is show in cross-section picture in Fig. 4.13. Thickness of the shell about 200 μm and average 1.6 mm diameter.

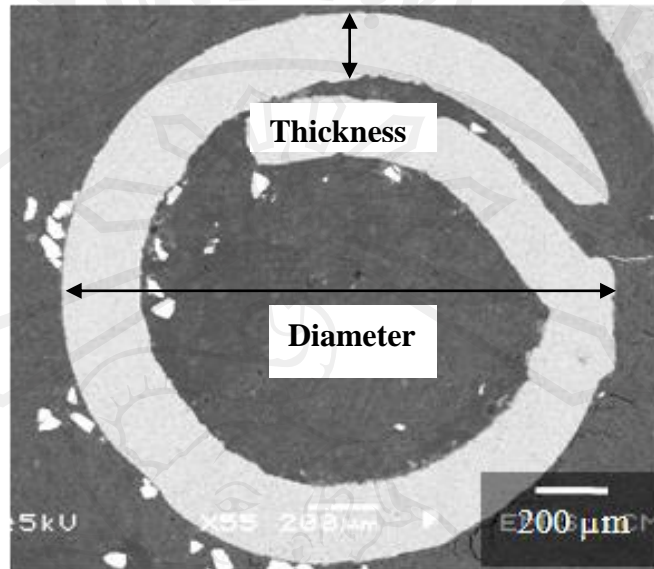


Figure 4.13 BSE-SEM micrograph of cross-section WC-Cr-Ni cored wires.

Chemical compositions of shell observed by EDS-SEM. It was found that Ni and Cr at 78.7 and 21.3 (wt%), respectively. Spectrum of EDS analysis as shown in Fig. 4.14.

Morphological analysis of fillers of WC-Cr-Ni cored wires reveals irregular shape particles, as shown in Fig. 4.14(a), and wide distribution. At high magnification level, it was found that each filler consists lots of tiny stick-shaped particles ($< 2 \mu\text{m}$) which form large particles as shown in Fig. 4.14 (c).

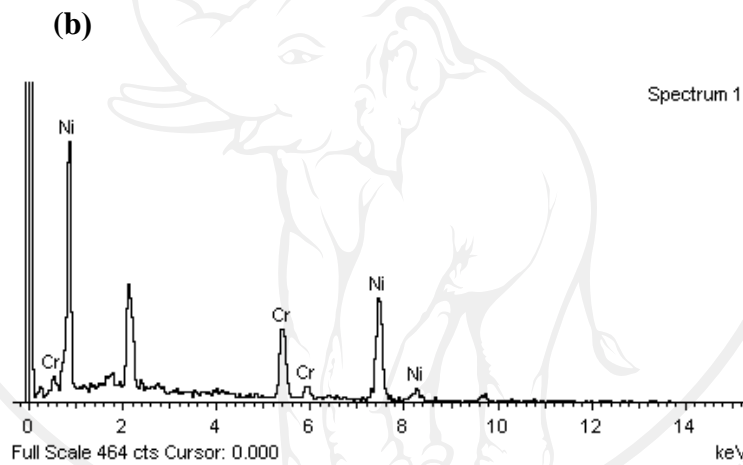
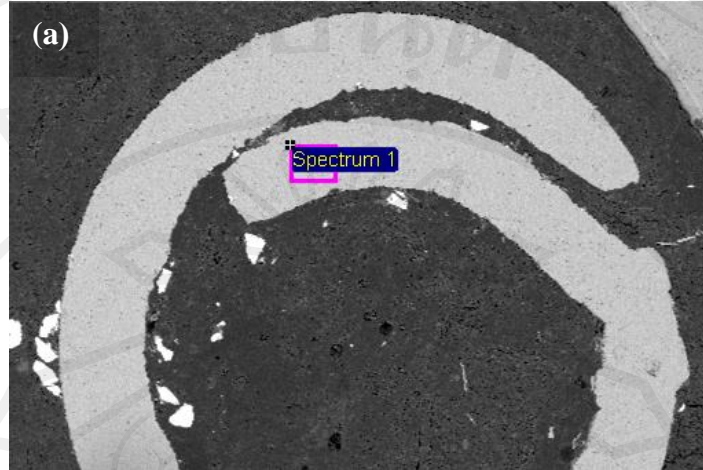


Figure 4.14 (a) SE-SEM micrograph of WC-Cr-Ni shell and (b) EDS spectrum of WC-Cr-Ni shell.

Analysis of particle size of WC-Cr-Ni fillers showed that size distribution was in the range of 0.1 to 110 μm with the mean size of 40 μm as shown in Fig. 4.16.

Chemical compositions of the filler of WC-Cr-Ni cored wire by EDS-SEM showed W and C as main element at 93.0 and 7.0 weight percent respectively. EDS spectrum is shown analysis in Fig. 4.17.

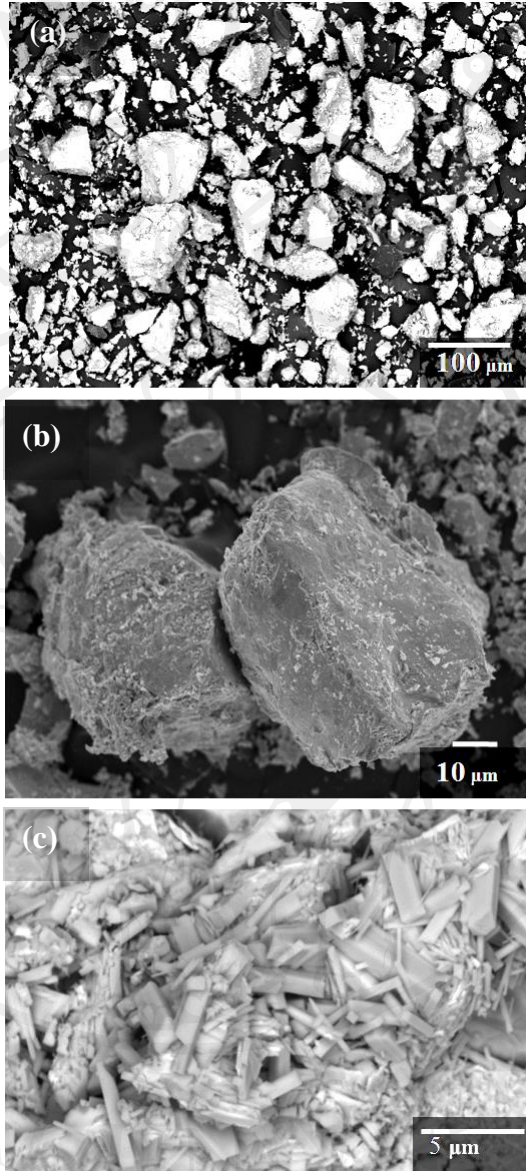


Figure 4.15 SE-SEM micrograph of WC-Cr-Ni filler at (a) 500X, (b) 1000X, and (c) 5000X.

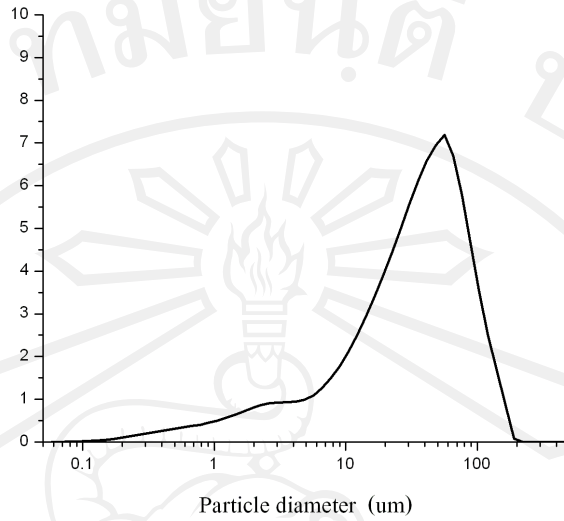


Figure 4.16 Size distribution of filler particle of WC-Cr-Ni cored wire.

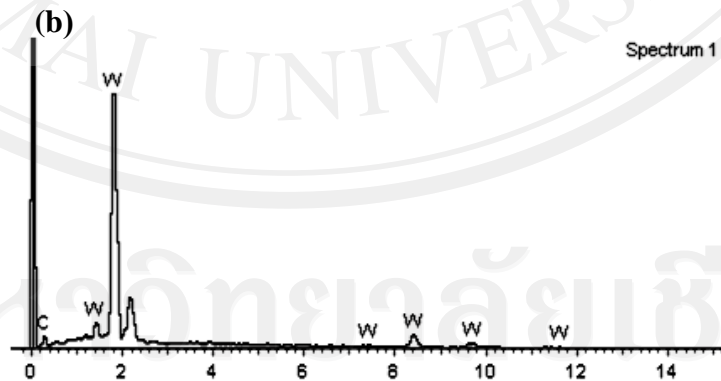
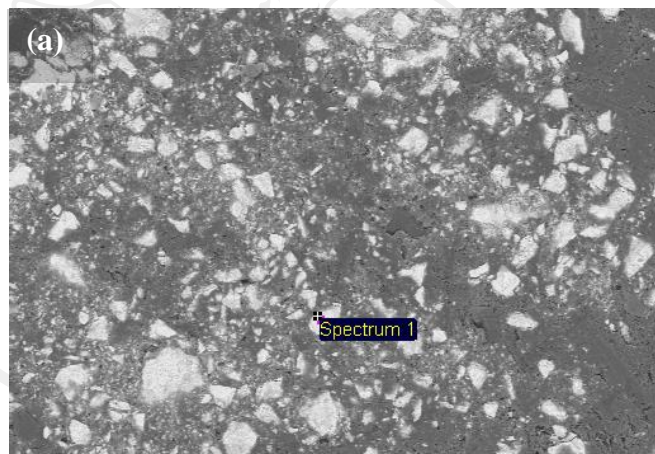


Figure 4.17 (a) BSE-SEM micrograph of WC-Cr-Ni filler particle and (b) EDS spectrum of filler particle.

Phase compositions of the fillers of WC-Cr-Ni cored wire identified by XRD technique showed WC and W_2C as principal phases (Fig. 4.18).

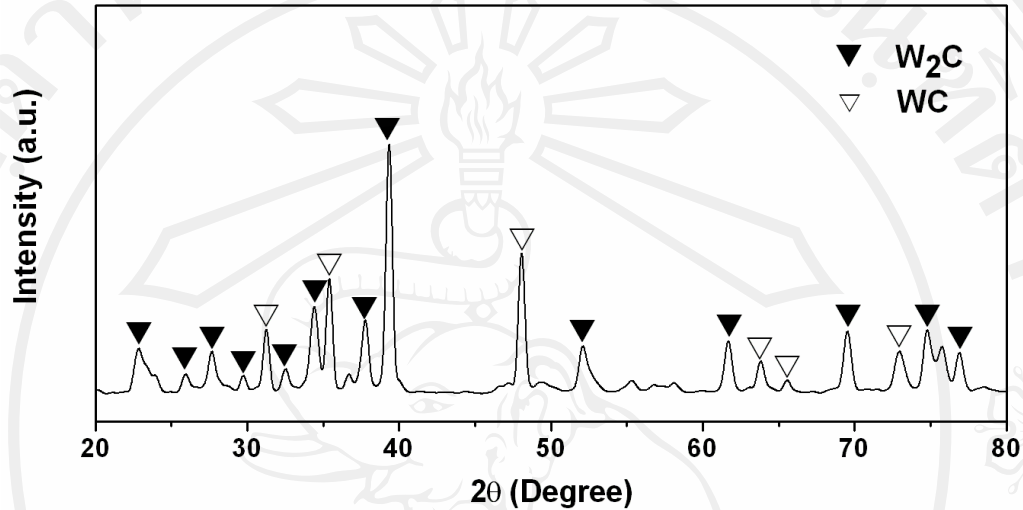


Figure 4.18 X-ray diffraction patterns of filler of WC-Cr-Ni.

4.2.2 WC-Cr-Fe cored wire

Fig. 4.19 shows cross-section of WC-Cr-Fe outer shell. Thickness of the shell was about 300 μm with an average diameter of 2 mm

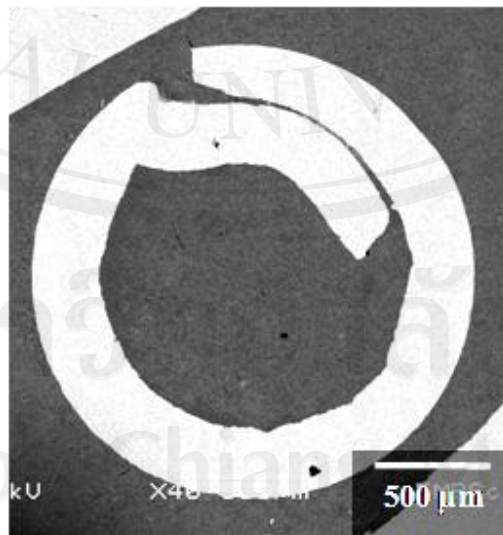


Figure 4.19 BSE-SEM micrograph shows cross-section of WC-Cr-Fe cored wire.

Chemical compositions of WC-Cr-Fe cored wire consisted of Fe as a major element at 67.3 (wt %) along with Cr, Ni, and C at 19.5, 9.0 and 7.2 respectively. Spectrum of WC-Cr-Fe shell analyzed by EDS as shown in Fig. 4.20

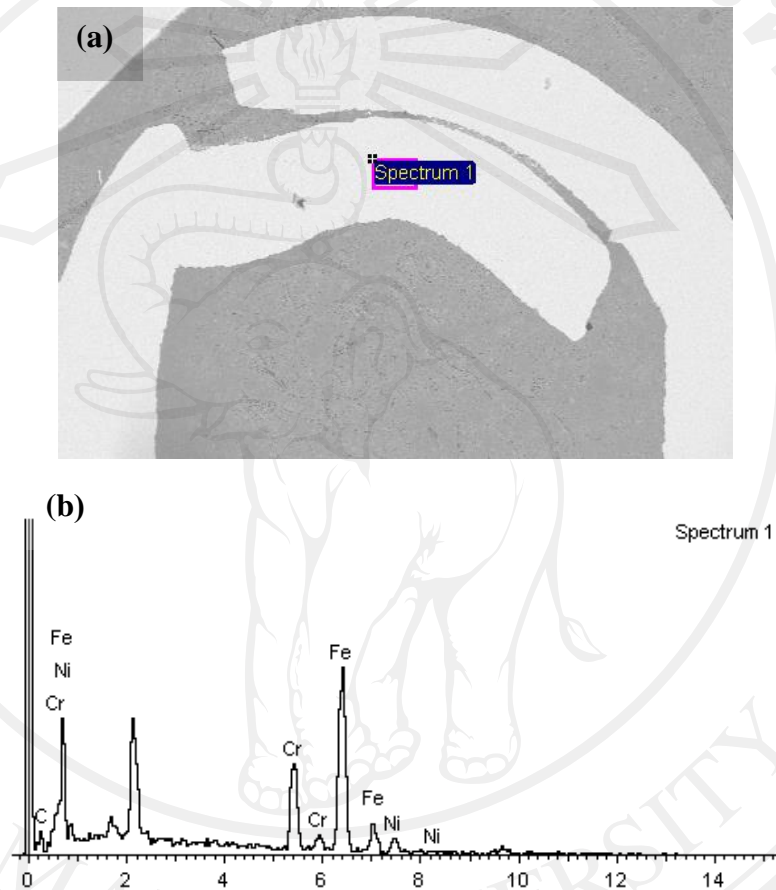


Figure 4.20 (a) BSE-SEM micrograph and (b) EDS spectrum of WC-Cr-Fe shell.

Fig. 4.21 shows morphology of WC-Cr-Fe filler particle as irregular shape. Filler particle had size distribution in a range of 0.2 - 130 μm with the average diameter of 53 μm .

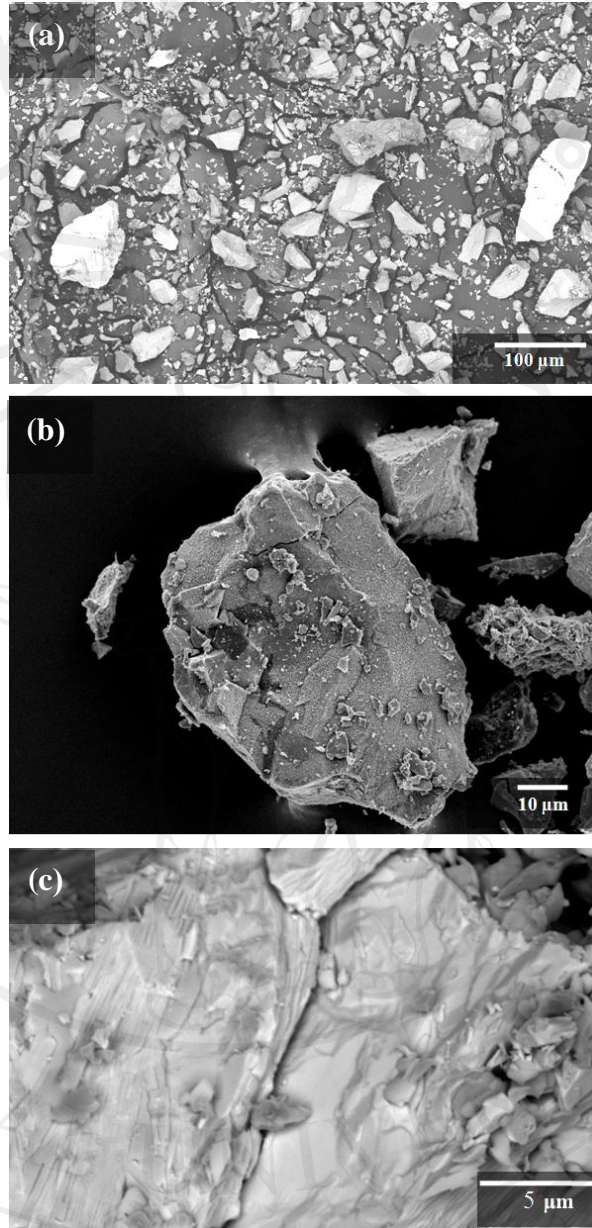


Figure 4.21 SE-SEM micrograph of WC-Cr-Fe fillers at (a) 500X, (b) 1000X and (c) 5000X magnifications.

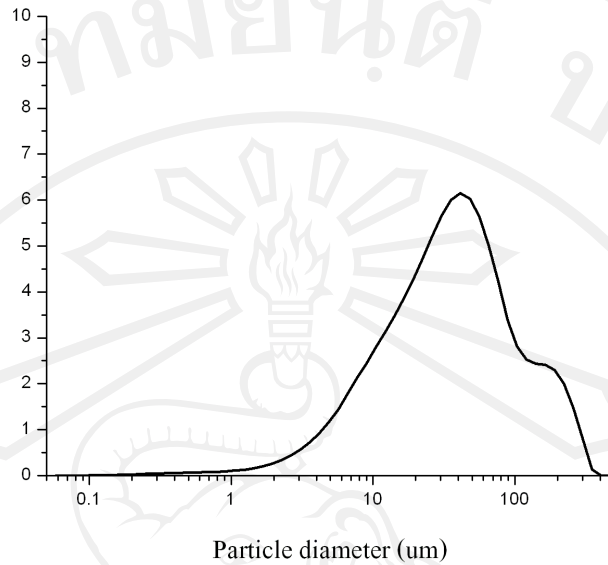


Figure 4.22 Size distribution of filler particle of WC-Cr-Fe cored wire.

Chemical compositions of WC-Cr-Fe fillers are shown in Fig. 4.23. The W was found as main component in the first area (74.4 wt%) while Fe was found as main component (48.2 wt%) in the second area along with other substances, as shown in Table 4.7. Spectrum of EDS analysis as shown in Fig. 4.23 (a) and (b).

Table 4.7 Chemical compositions of WC-Cr-Fe cored wire filler by EDS analysis.

| Element | area 1 | | area 2 | |
|---------|--------|------|--------|------|
| | wt% | at% | wt% | at% |
| W | 74.4 | 21.6 | - | - |
| Fe | 5.2 | 5.0 | 48.2 | 16.2 |
| O | 15.3 | 50.9 | 3.17 | 3.70 |
| C | 5.1 | 22.5 | 20.6 | 32.0 |
| B | 28.0 | 48.3 | - | - |

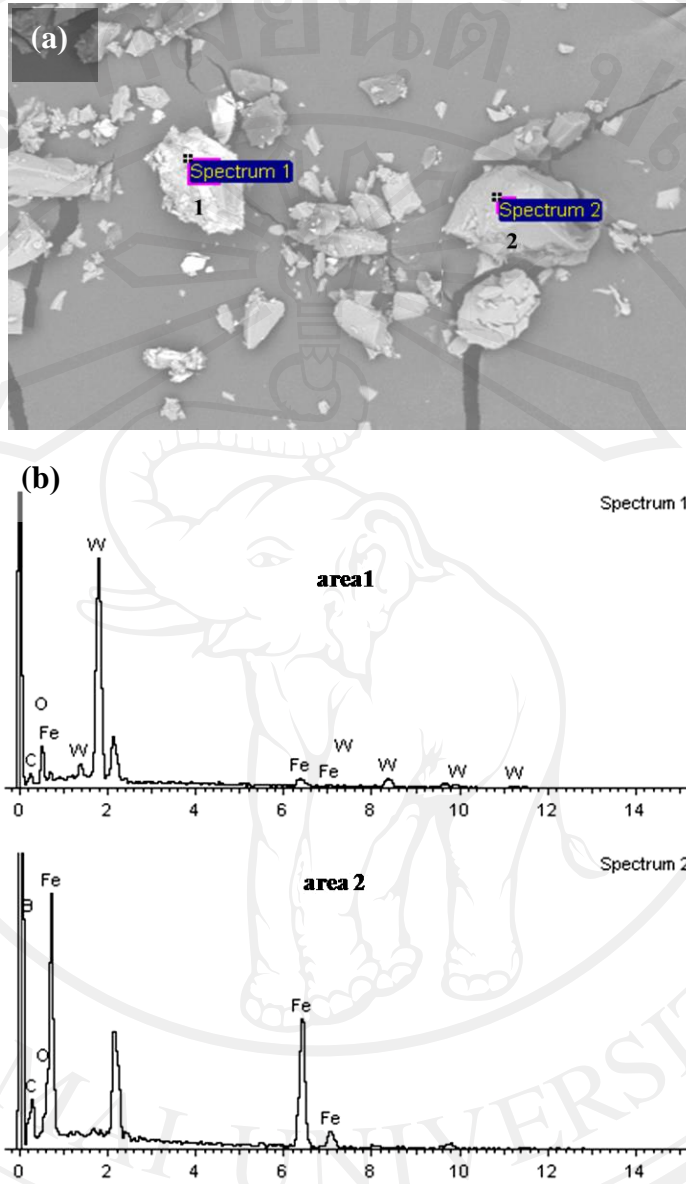


Figure 4.23 (a) SEM micrograph of WC-Cr-Fe filler (b) and (c) EDS spectrum of area 1 and area 2.

Phase identification of WC-Cr-Fe cored wire by XRD technique showed WC, W_2C , FeB and Ni as shown in Fig. 4.24.

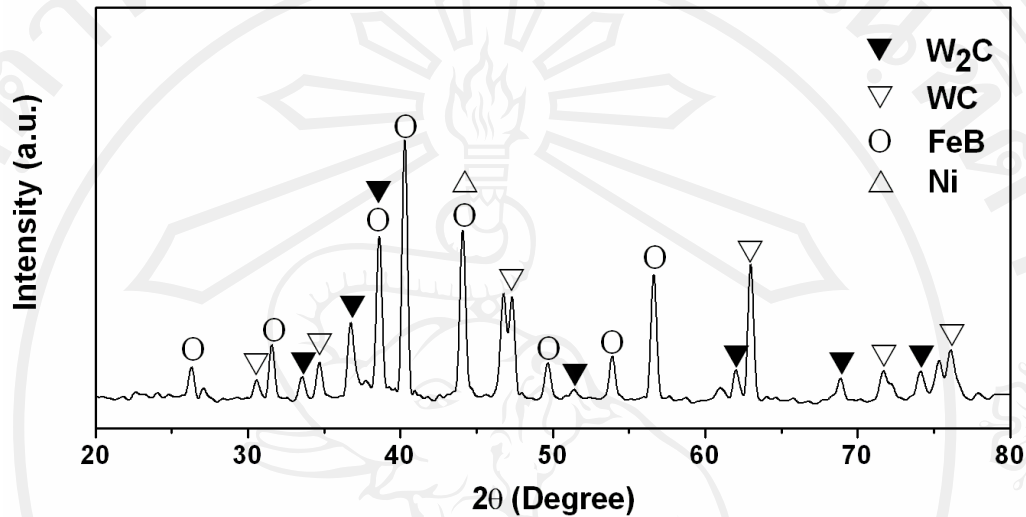


Figure 4.24 X-ray diffraction patterns of the filler particle of WC-Cr-Fe cored wire.

4.2.3 W-Cr-Fe nanocomposite cored wires

W-Cr-Fe nanocomposite cored wire consists of shell and filler. The shell was about 200 μm thick and diameter of 1.6 mm as showed in Fig. 4.25. Analysis of chemical compositions of W-Cr-Fe nanocomposite cored wires shown Fe, Cr element as a main components about 82.6 and 17.4 (wt%), respectively. Spectrum of W-Cr-Fe nanocomposite cored wires shell from EDS analysis as shown in Fig. 4.26.

The morphological analysis of W-Cr-Fe nanocomposite fillers found widely-distributed irregular shaped particles, as shown in Fig. 4.27. Most particles have diameters of 52 μm . Size distribution range from 0.2 to 125 μm , as shown in Fig. 4.28.

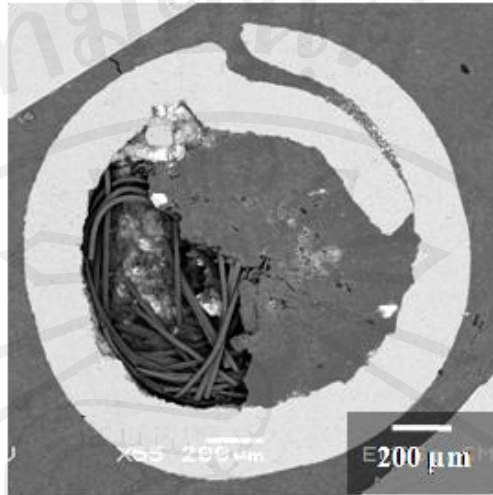


Figure 4.25 BSE-SEM micrograph shows cross section of W-Cr-Fe nanocomposite cored wire.

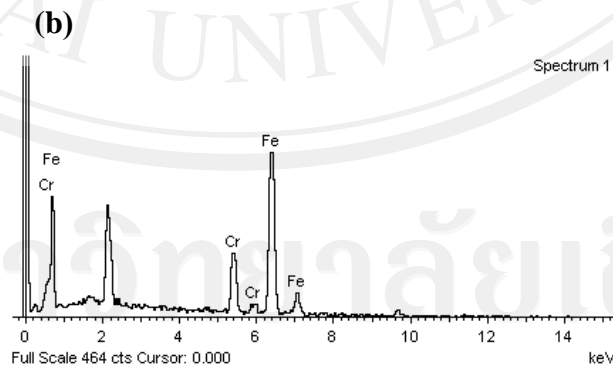
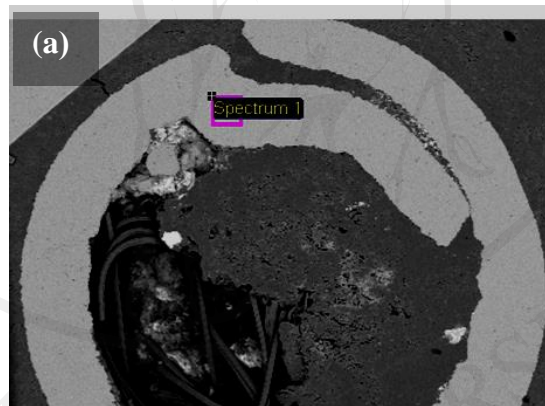


Figure 4.26 (a) BSE-SEM micrograph and (b) EDS spectrum of W-Cr-Fe nanocomposite shell.

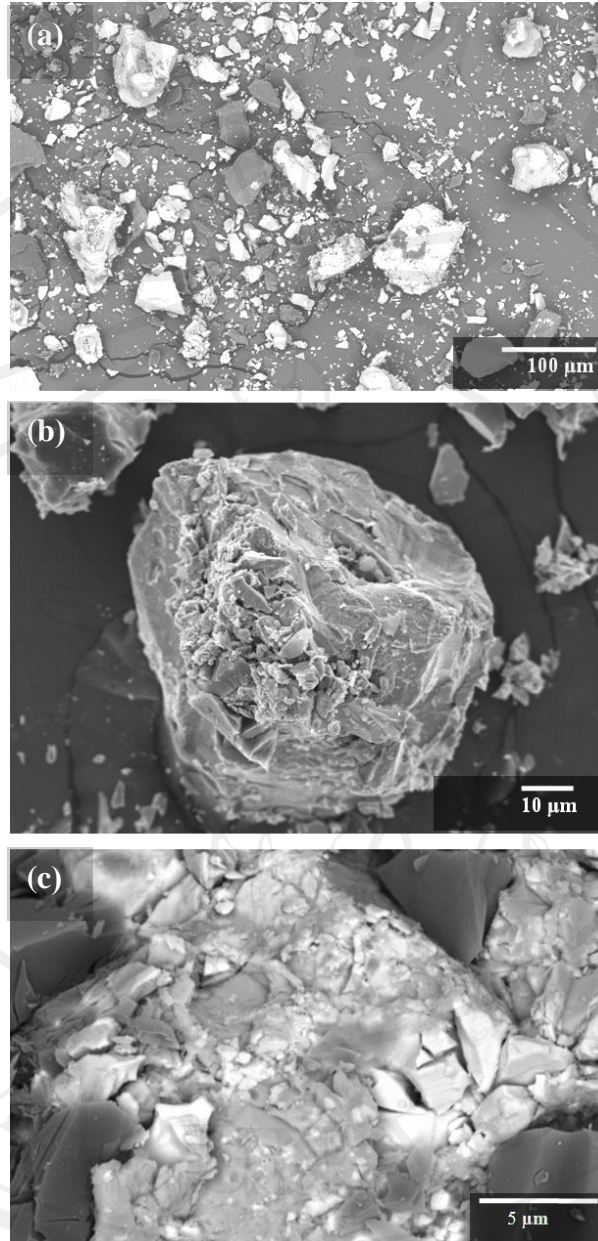


Figure 4.27 SE-SEM micrographs show morphology of W-Cr-Fe nanocomposite filler at (a) 500X (b) 1000X and (c) 5000X magnification.

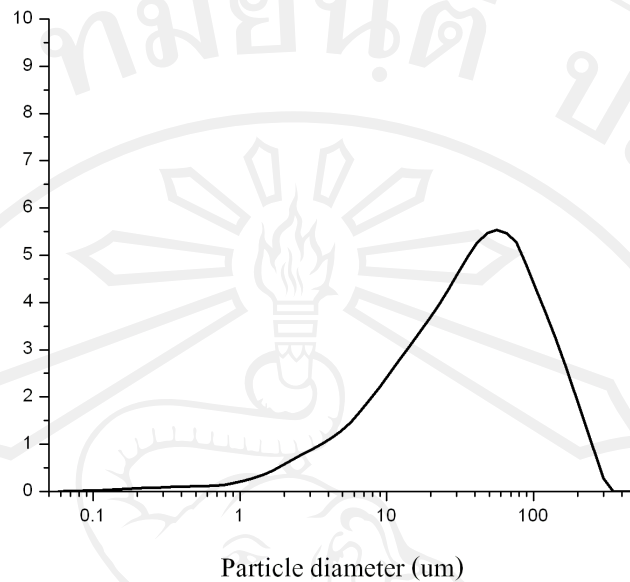


Figure 4.28 Size distribution of filler particle of W-Cr-Fe nanocomposite cored wire.

Phase compositions of W-Cr-Fe nanocomposite fillers by EDS-SEM (Fig. 4.29) showed 3 principal phases from difference areas. EDS-SEM analysis area 1 showed W as a main element at 94.0 wt%. Cr and Fe were found as main element of area 2 at 61.4 and 20.7 wt%, respectively. Fe and Nb were found main element of area 3 at 14.7 and 62.0 wt%, respectively. EDS spectrums are shown in Fig. 4.29 (b-d) and results are shown in Table 4.8.

Table 4.8 Chemical compositions of W-Cr-Fe nanocomposite filler analyzed by EDS-SEM.

| Element | area1 | | area2 | | area3 | |
|---------|-------|------|-------|------|-------|------|
| | wt% | at% | wt% | at% | wt% | at% |
| W | 94.0 | 54.4 | - | - | - | - |
| Cr | - | - | 61.4 | 59.6 | - | - |
| C | 2.6 | 22.7 | 2.9 | 12.1 | 9.3 | 26.5 |
| O | 3.5 | 23.0 | 0.5 | 1.7 | 1.7 | 26.5 |
| Fe | - | - | 20.7 | 18.7 | 14.7 | 9.0 |
| Nb | - | - | 14.5 | 7.9 | 62.0 | 22.9 |
| B | - | - | - | - | 11.5 | 37.4 |

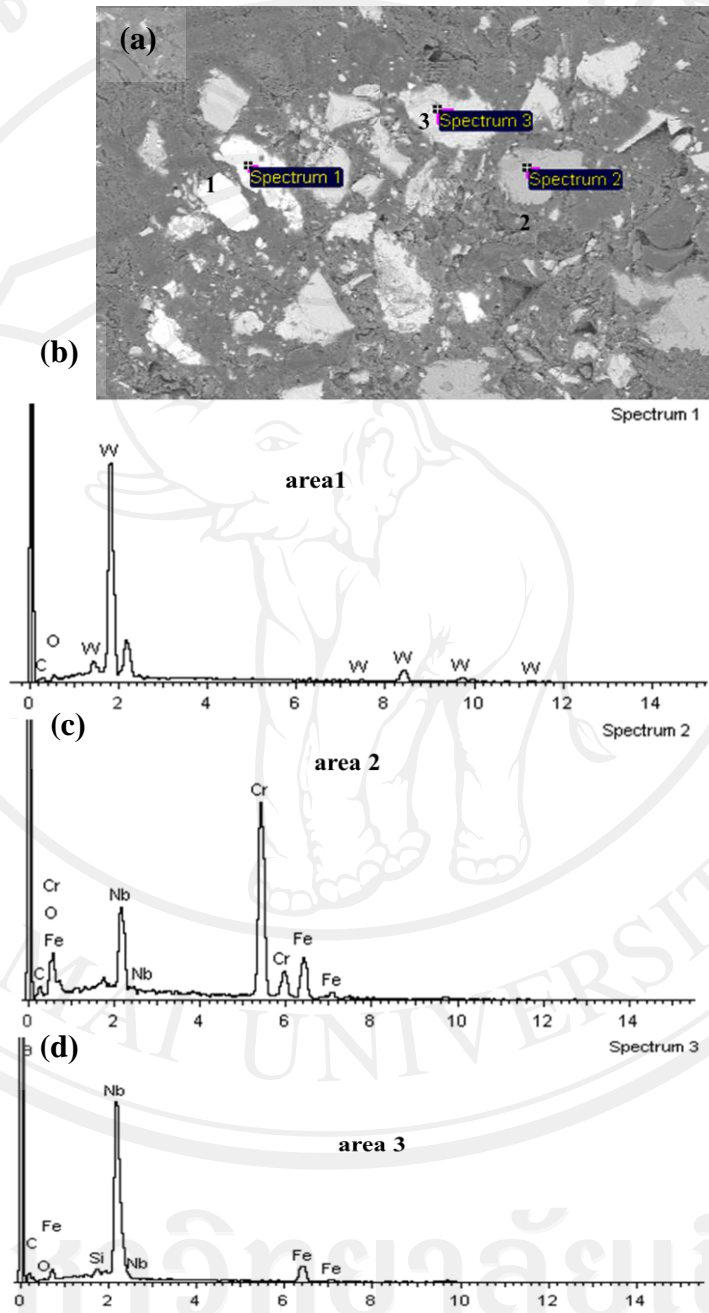


Figure 4.29 (a) BSE-SEM micrograph and (b) EDS spectrums of area 1,2 and 3 of W-Cr-Fe nanocomposite filler.

Different phases found in W-Cr-Fe nanocomposite cored wires filler by X-ray diffraction (XRD) including WC, W_2C , Fe_2O_4 , FeNb, B_4C , and FeCr as shown in Fig. 4.30.

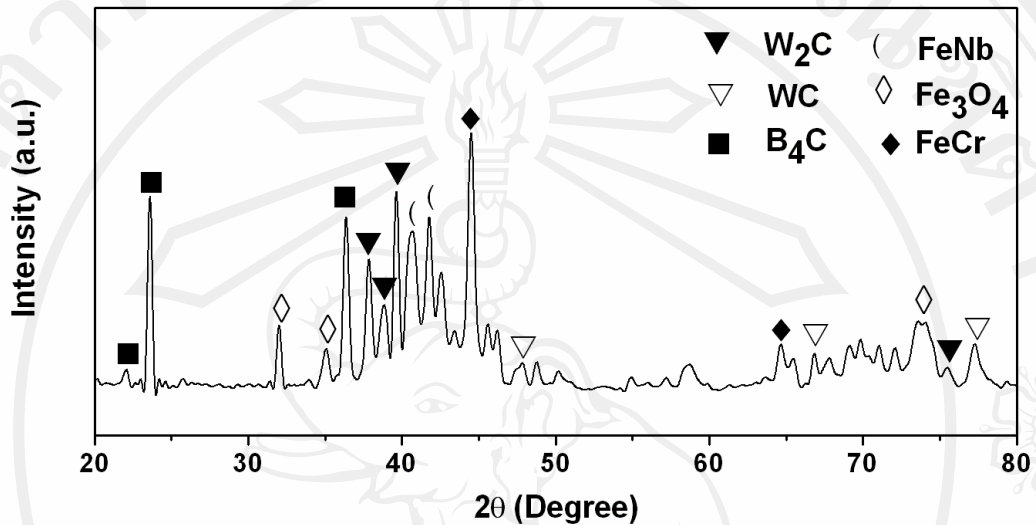


Figure 4.30 X-ray diffraction patterns of the filler of W-Cr-Fe nanocomposite cored wire.

4.2.4 Summary of characteristics of spray materials

All cored wires consisted of outer metallic shell having similar thickness ranging in the range of 250-300 μm . Filler particles size distribution is compared in Fig. 4.31 with the average particle diameter shown in Table 4.9.

Chemical compositions of metallic shells and filler particles were analyzed by EDS are summarized in Table 4.9.

Phase analysis of filler particle by XRD showed that WC and W_2C as major hard phase presented in all filler types as shown in Fig. 4.32. For WC-Cr-Fe filler, carbide phases were typically found as WC and W_2C . The W-Cr-Fe nanocomposite filler particles

showed complexity of present phase, composed of carbide and hard metallic phase with nanostructure.

Table 4.9. Comparison of cored wires characteristics.

| Type of cored wires | WC-Cr-Ni | WC-Cr-Fe | W-Cr-Fe nanocomposite |
|---|----------------------|----------------------------------|--|
| Outer shell thickness (μm) | 200 | 300 | 200 |
| Outer shell compositions | Ni, Cr | Fe,Cr,Ni,C | Fe,Cr |
| Filler size range ($\varnothing,\mu\text{m}$) | 0.1-110 | 0.2-130 | 0.2-125 |
| Filler average diameter (μm) | 40 | 53 | 52 |
| Filler compositions | W, C | W, Fe, B,C | W, Cr, Fe ,Nb,B,C |
| Filler phases | WC, W ₂ C | WC, W ₂ C, FeB, Ni | WC, W ₂ C, B ₄ C, FeNb, Fe ₃ O ₄ , FeCr |

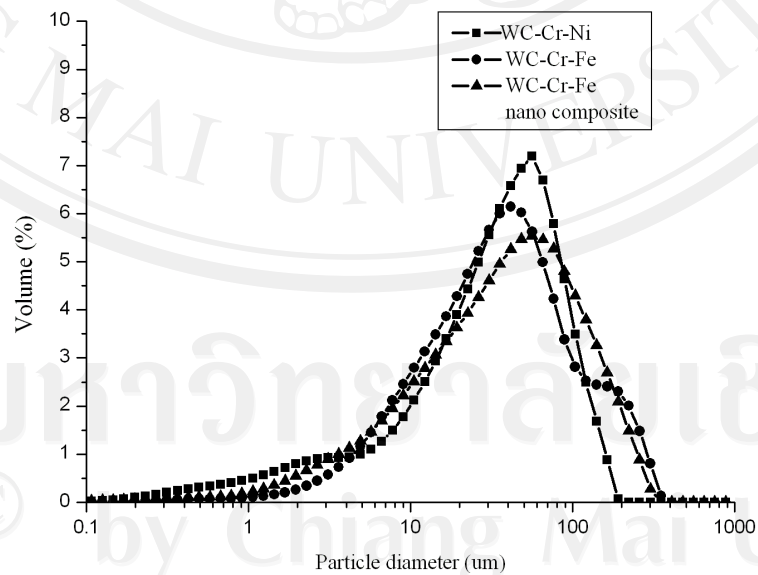


Figure 4.31 Graph showing distribution of fillers size.

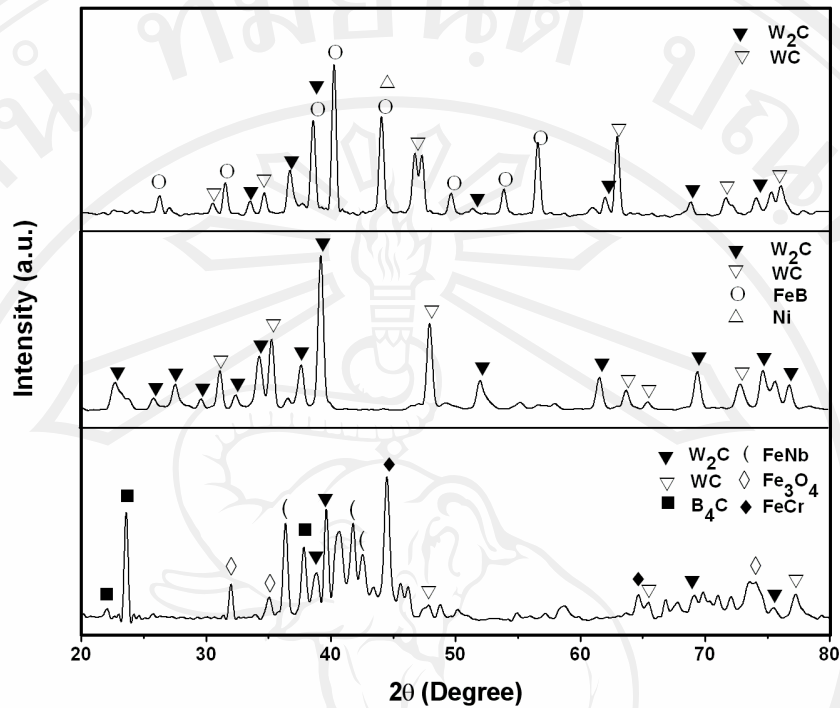


Figure 4.32 X-ray diffraction patterns of: (a) WC-Cr-Ni; (b) WC-Cr-Fe; (c) W-Cr-Fe nanocomposite fillers.

4.3 Characteristics of in-flight particle

Characterizations of in-flight particle include size, morphology, microstructure, chemical compositions, and phase compositions. Details are as follow:

4.3.1 In-flight particle from WC-Cr-Ni cored wire

Morphology of the in-flight particle from WC-Cr-Ni cored wire was a spherical shape, as shown in Fig. 4.33. This indicates fusion of metal shell occurred during spray process. SE-SEM micrograph at high magnification showed rough surface of carbide particles.

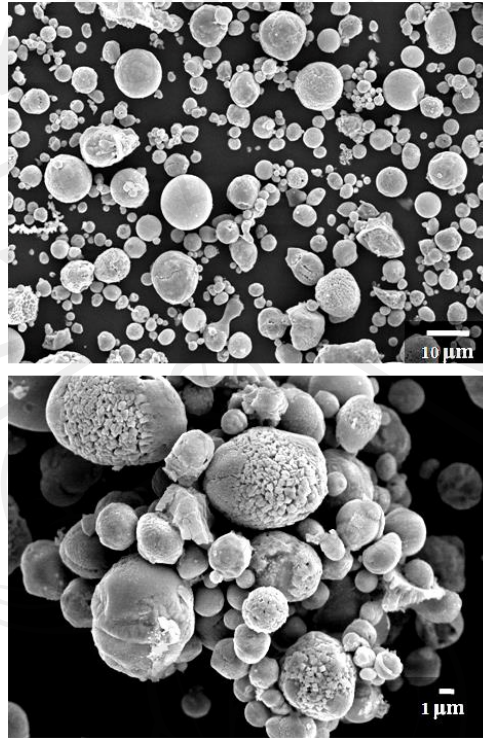


Figure 4.33 SE-SEM micrograph of in-flight particle from WC-Cr-Ni core wire.

Size distribution of the in-flight particle was in the range of 0.8 to 58 μm with the mean size of 12.3 μm (Fig. 4.34).

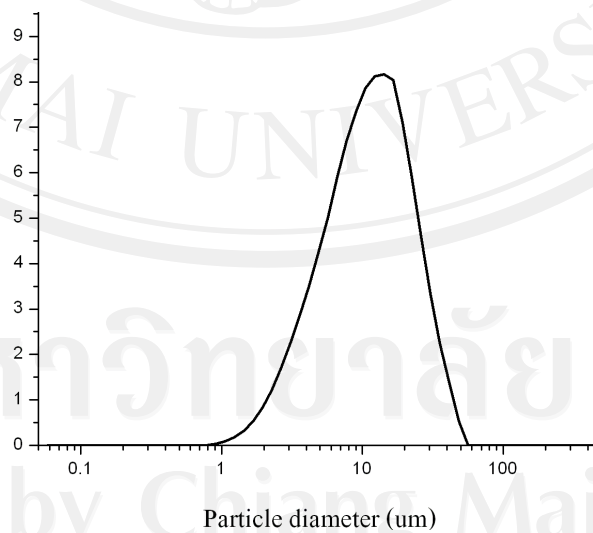


Figure 4.34 Size distribution of in-flight particle from WC-Cr-Ni core wire.

Fig. 4.35 Shows BSE-SEM cross sectioned image of WC-Cr-Ni in-flight particle indicated as area1 area2 and area3 for EDS analysis. Chemical composition revealed by EDS-SEM was shown as spectrums in Fig. 4.36, along with quantitative analysis results shown in table 4.10. In-flight particles were produced by fusion of metal shell and cermets fillers of the cored wire with was principal phase composition.

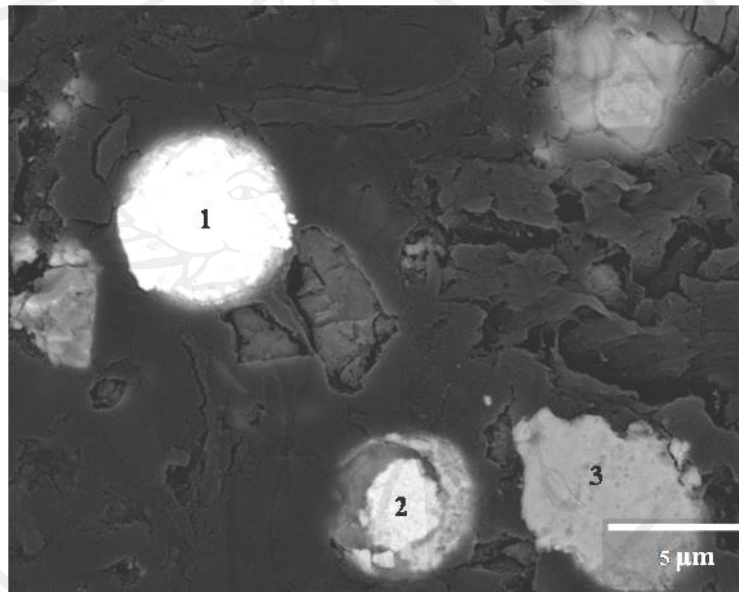


Figure 4.35 BSE-SEM micrograph of cross-sectioned WC-Cr-Ni in-flight particle.

Table 4.10 Chemical compositions of WC-Cr-Ni in-flight particle.

| Element | area1 | | area2 | | area3 | |
|---------|-------|------|-------|------|-------|------|
| | wt% | at% | wt% | at% | wt% | at% |
| W | 77.8 | 19.7 | 49.9 | 11.1 | 21.3 | 6.4 |
| Ni | 5.3 | 4.4 | 30.4 | 21.3 | 62.2 | 58.6 |
| Cr | 1.48 | 1.4 | - | - | 11.5 | 12.3 |
| C | 18.4 | 74.5 | 19.6 | 67.6 | 4.9 | 22.8 |

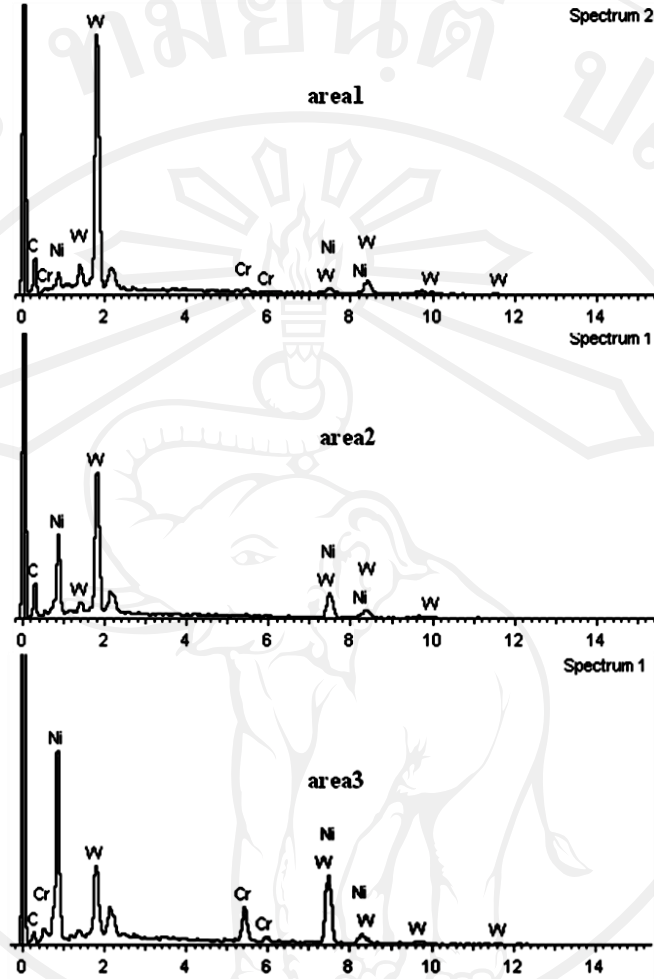


Figure 4.36 EDS spectrum of WC-Cr-Ni in-flight particles taken from area1, area2 and area3, respectively (Fig. 4.35).

Phase analysis of WC-Cr-Ni in-flight particle using X-ray diffraction showed different phases including W_2C , Cr, and Ni as shown in Fig. 4.37.

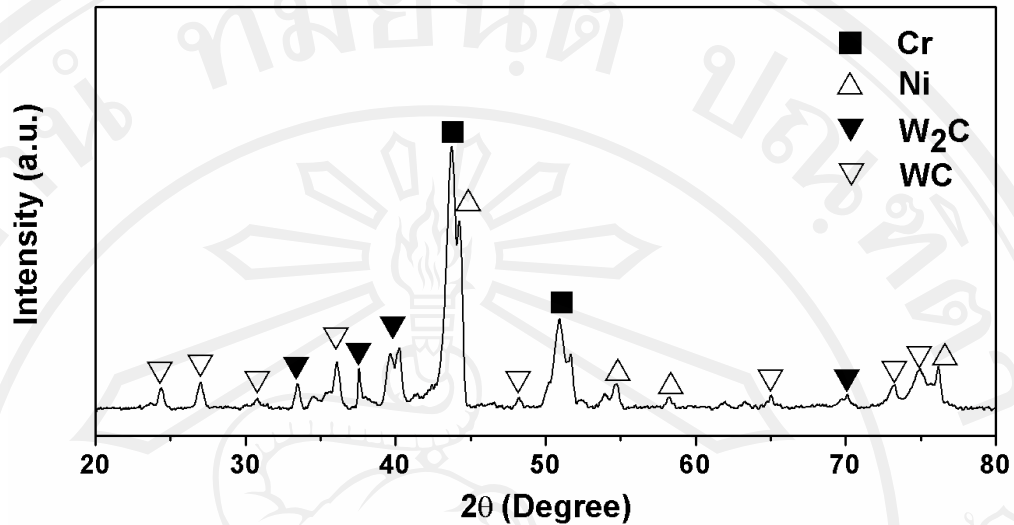


Figure 4.37 X-ray diffraction patterns of WC-Cr-Ni in-flight particles.

4.3.2 In-flight particle from WC-Cr-Fe cored wire

Morphology of in-flight particle from WC-Cr-Fe cored wire shown by SEM as spherical shape with some smooth and rough surfaces as shown in Fig. 4.38. Particle size distribution was in the range of 0.8 to 80 μm as shown in Fig. 4.39 with the mean size of 17.5 μm .

Cross-section of WC-Cr-Fe in-flight particle by using BSE-SEM technique shows difference in brightness which indicates difference in composition of each particle, as shown in Fig. 4.40 EDS analysis of chemical compositions in the area1, area, and area3 yielded EDS spectrum as shown in Fig. 4.41 with details in Table 4.11. The brightest in flight particle consisting essentially of W (area1) which comes from the filler in the cored wires. The less bright in flight particle with a combination of Fe and Cr mainly (area1 and 2) which derived from the melting of the filler and shell of the core wire. Apparently, there is a separate of WC in filler because the arc and incomplete melted which will affect to the coating.

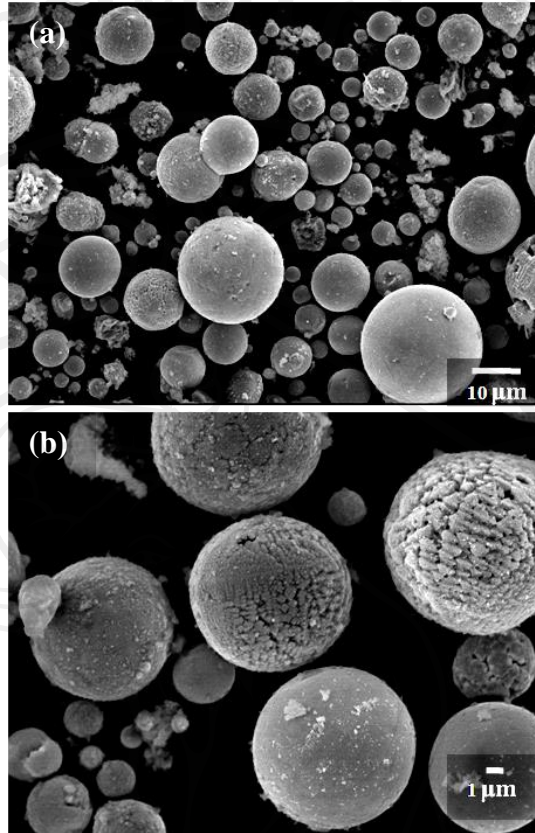


Figure 4.38 SE-SEM micrographs of WC-Cr-Fe in-flight particle at (a) 1000X and (b) 3500X magnifications.

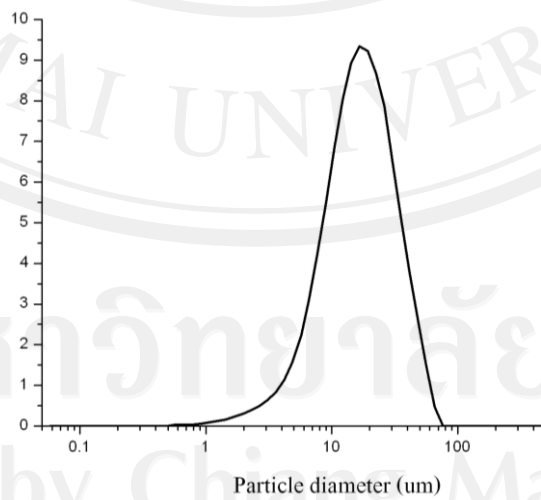


Figure 4.39 Size distribution of in-flight particles from WC-Cr-Fe core wire.

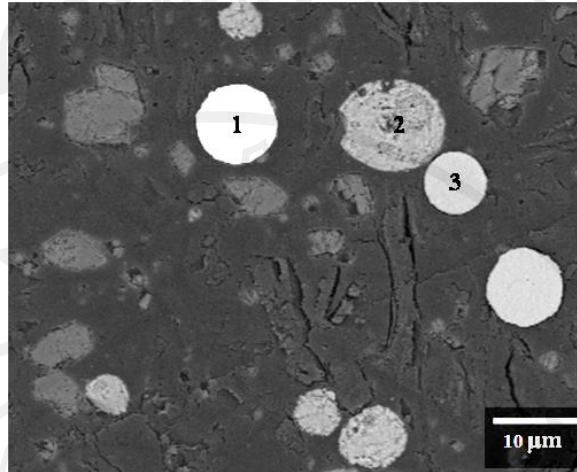


Figure 4.40 BSE-SEM micrograph of cross-section WC-Cr-Fe in-flight particle.

Table 4.11 Chemical compositions of WC-Cr-Fe in-flight particle.

| Element | area1 | | area2 | | area3 | |
|---------|-------|------|-------|------|-------|------|
| | wt% | at% | wt% | at% | wt% | at% |
| W | 84.4 | 46.1 | 3.0 | 0.5 | - | - |
| Ni | 8.9 | 15.2 | 3.6 | 1.8 | 4.5 | 4.2 |
| Cr | 2.7 | 5.2 | 9.4 | 5.2 | 14.5 | 15.4 |
| C | 4.0 | 33.6 | 3.8 | 9.1 | - | - |
| Fe | - | - | 47.0 | 24.4 | 81.0 | 80.3 |
| O | - | - | 31.6 | 57.2 | - | - |

Phase analysis of WC-Cr-Fe in-flight particle by using X-ray diffraction shows the main phases of Fe_2O_4 , FeCr , FeNi , and FeCrNi which are common compound of Fe, as shown in Fig. 4.42. This phase that occurred in this system because component phase were occurred by current and arc between shell and cause fillers melted together.

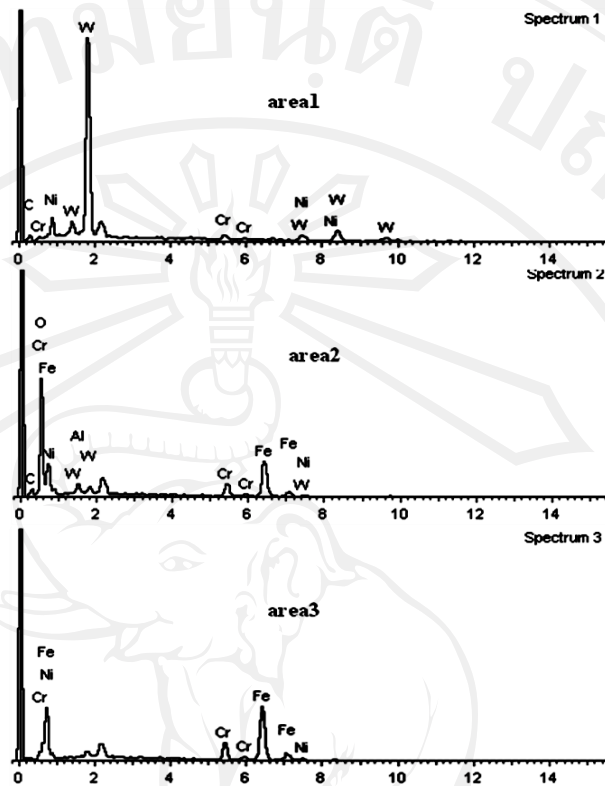


Figure 4.41 EDS Spectrums of WC-Cr-Fe in-flight particle taken from area1, area2 and area3 respectively (Fig. 4.40).

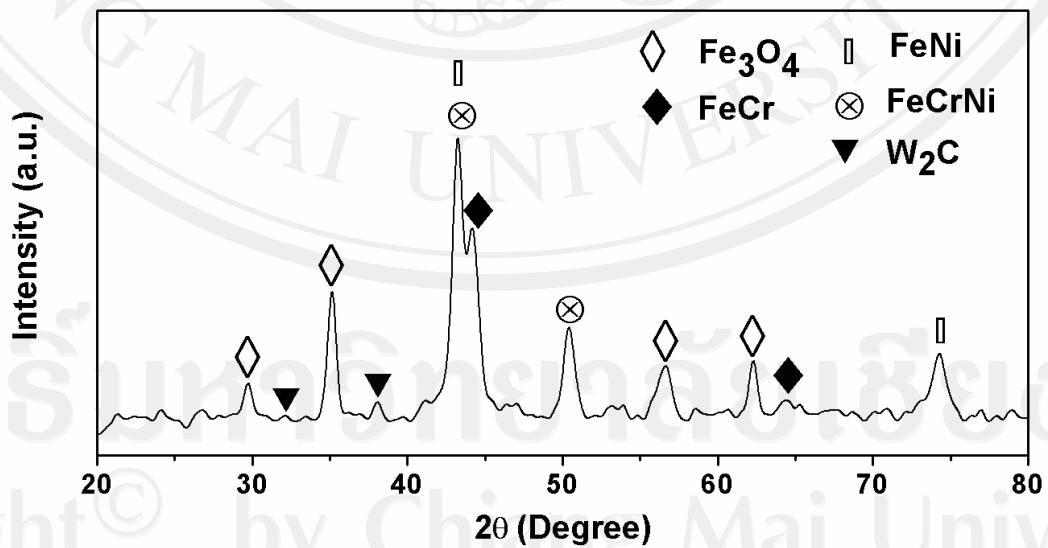


Figure 4.42 X-ray diffraction patterns of WC-Cr-Fe in-flight particles.

4.3.3 In-flight particle from W-Cr-Fe nanocomposite cored wire

Analysis of in-flight particle from W-Cr-Fe nanocomposite cored wire by using SEM microscope showed that in-flight particles are spherical shape with rather smooth particle surface compared to in-flight particles from other spray wires (Fig. 4.43). Nanostructure of cermet material could contribute in better fusion. The average diameter of W-Cr-Fe nanocomposite in-flight particles was $26.7 \mu\text{m}$, with particle size distribution ranging from 0.8 to $115 \mu\text{m}$ as shown in Fig. 4.44.

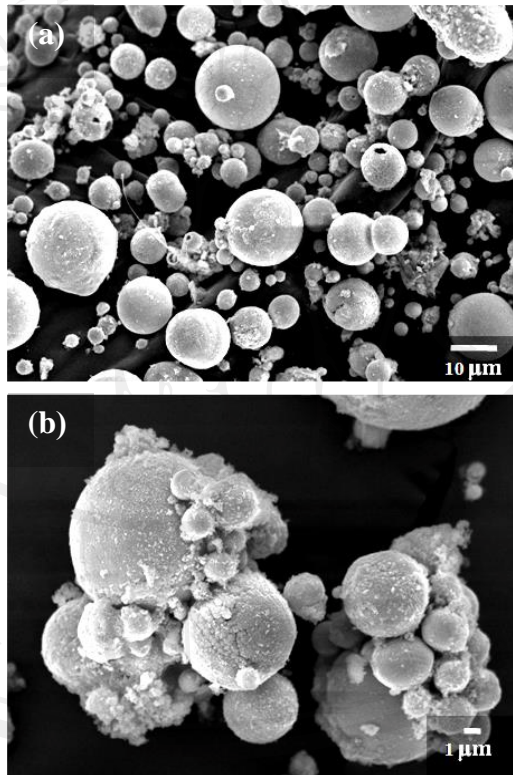


Figure 4.43 SE-SEM micrograph of W-Cr-Fe nanocomposite in-flight particle at (a) 1000X and (b) 3500X magnification.

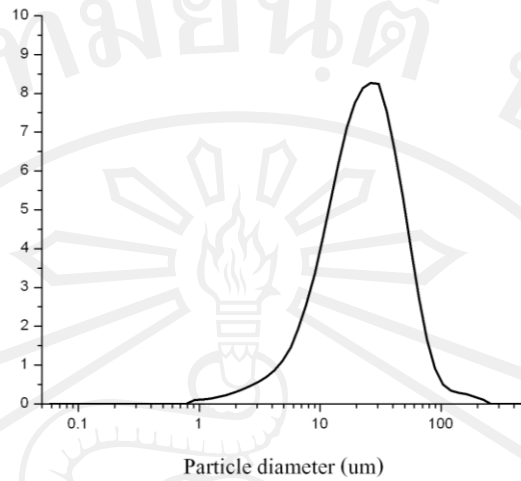


Figure 4.44 Size distribution of in-flight particles from W-Cr-Fe nanocomposite core wire.

Cross-sectioned image of W-Cr-Fe nanocomposite in-flight particle (Figure 4.45) shows good homogeneity of particles. EDS-SEM analysis of chemical compositions taken from area 1 and 2 were shown in Fig. 4.45. Fig. 4.46 shows EDS spectrum revealed that Fe, Cr, Nb, C and W were major components. Details of percentage are presented in Table 4.12.

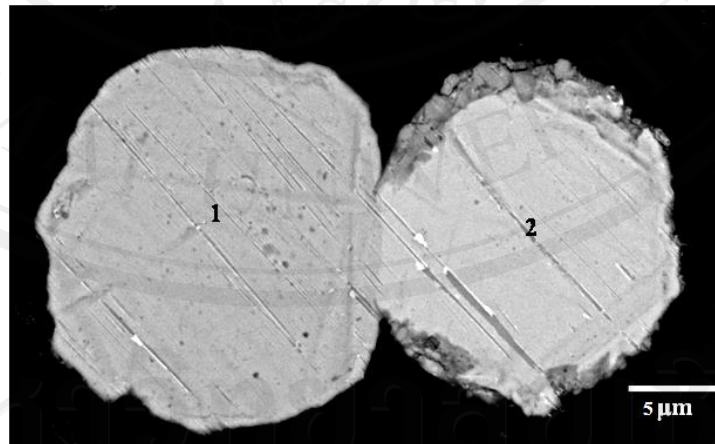


Figure 4.45 BSE-SEM micrograph of cross-sectioned W-Cr-Fe nanocomposite in-flight particle.

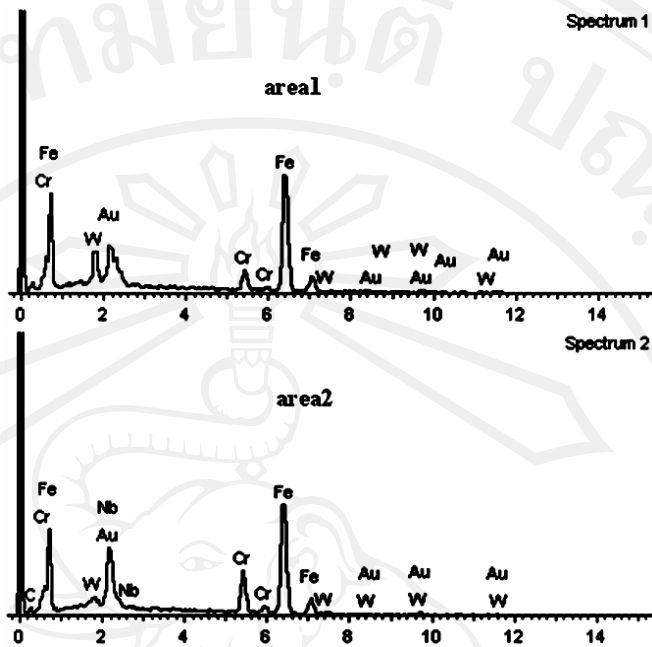


Figure 4.46 EDS spectrum of W-Cr-Fe nanocomposite in-flight particles taken from area 1 and 2 respectively from Fig. 4.45.

Table 4.12 Chemical compositions of W-Cr-Fe nanocomposite in-flight particles.

| Element | area 1 | | area 2 | |
|---------|--------|------|--------|------|
| | wt% | at% | wt% | at% |
| Fe | 64.2 | 65.1 | 72.6 | 84.4 |
| Cr | 13.1 | 14.7 | 7.0 | 8.7 |
| W | 1.6 | 0.5 | 10.5 | 3.7 |
| Nb | 8.4 | 5.1 | - | - |
| C | 2.5 | 11.7 | - | - |

Phase analysis of W-Cr-Fe nanocomposite in-flight particle by using X-ray diffraction showed principle phases as FeCr and Fe₂O₄. This is from high Fe content of wire filler and shell. X-ray diffraction pattern is also shown in Fig. 4.47.

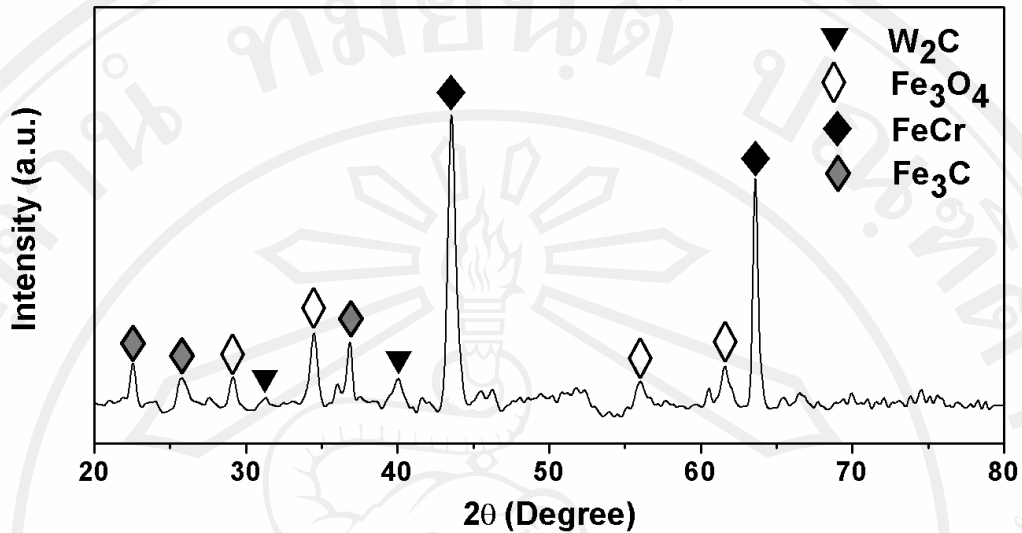


Figure 4.47 X-ray diffraction patterns of W-Cr-Fe nanocomposite in-flight particles.

4.3.4 Summary of characteristic of in-flight particles

The mean sizes of in-flight particles obtained by laser diffraction technique were 12 μm for WC-Cr-Ni, 18 μm for WC-Cr-Fe and 26 μm for W-Cr-Fe nanocomposite. The WC-Cr-Fe nanocomposite core wire, although having similar mean size of filler particles as WC-Cr-Fe, could have benefit of finer structure and higher metal content, resulted in high homogeneity and well melted in-flight particle. This benefit led to larger mean size of W-Cr-Fe nanocomposite in-flight particles, produced as shown in Fig. 4.48.

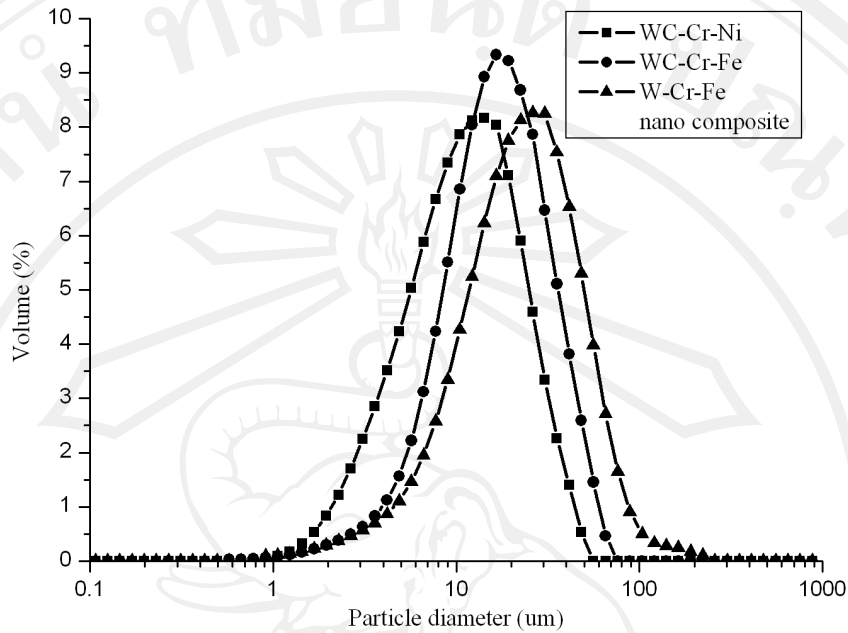


Figure 4.48 Graph showing distribution of in-flight particles size.

Morphology of the in-flight particles was revealed by SE-SEM micrographs along with BSE-SEM micrographs of their cross-sections. WC-Cr-Ni in-flight particles, W-rich and Ni-rich were typically found. For WC-Cr-Fe in-flight particles, W-rich and Fe-Cr-rich were exhibited. In contrast, W-Cr-Fe nanocomposite in-flight particles, the difference in phase composition of different particles was not easily distinguished by BSE-SEM micrographs as shown. Fe-Cr-rich was a typical phase identified by EDS-SEM as shown in Fig. 4.49

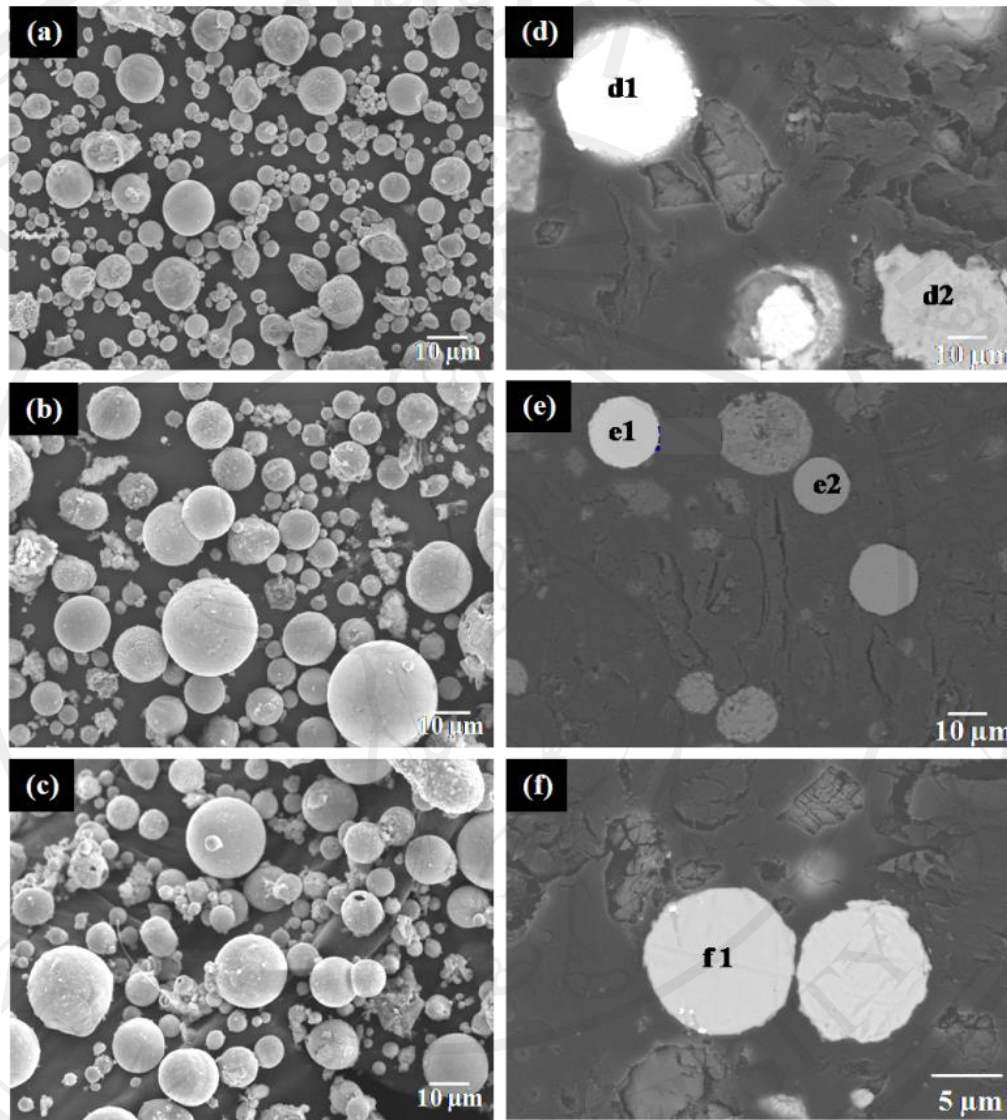


Figure 4.49 In-flight particle morphology by SE-SEM (a-c) and cross sections by BSE-SEM (d-f) of: (a,d) WC-Cr-Ni; (b,e) WC-Cr-Fe; (c,f) W-Cr-Fe nano-composite.

Phase analysis of in-flight particles by XRD showed that W_2C was typically found in all in-flight types as shown in Fig. 4.50. As expected, Ni and Cr were found in the outer shell of WC-Cr-Ni core wire, presented in the in-flight particles. Multi-phase was presented

in filler particle of WC-Cr-Fe core wire, also exhibited in the in-flight particle, including W_2C , Fe_3O_4 , FeNi, and FeCrNi phases. For W-Cr-Fe nanocomposite in-flight particle, W_2C , Fe_3O_4 , FeCr and FeNb phase were detected while the absence of WC could be as a result of decarburization of W_2C [32, 35, 36].

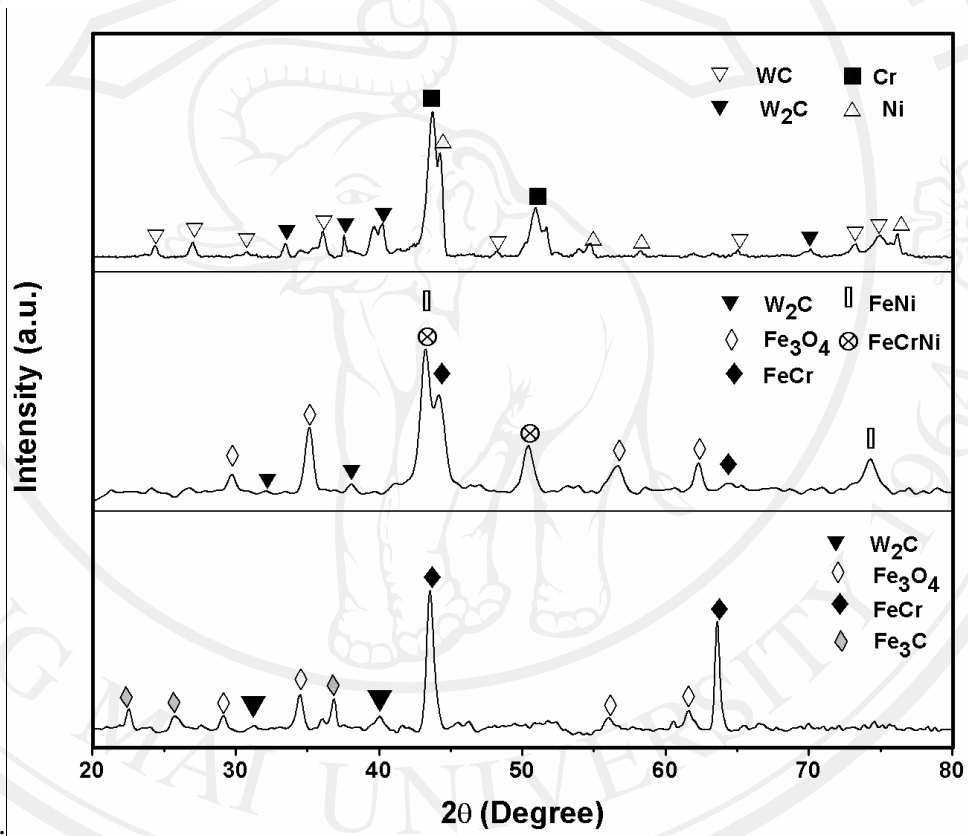


Figure 4.50 XRD patterns of in-flight particles: (a) WC-Cr-Ni; (b) WC-Cr-Fe; (c) W-Cr-Fe nanocomposite.

Cross section of in-flight particles was revealed by SEM and FIB technique, found two types of in-flight particle, pore and solid structure. Each particle consists of fine eutectic structures that were from solidification process as shown in Fig. 4.51 [6,12,58].

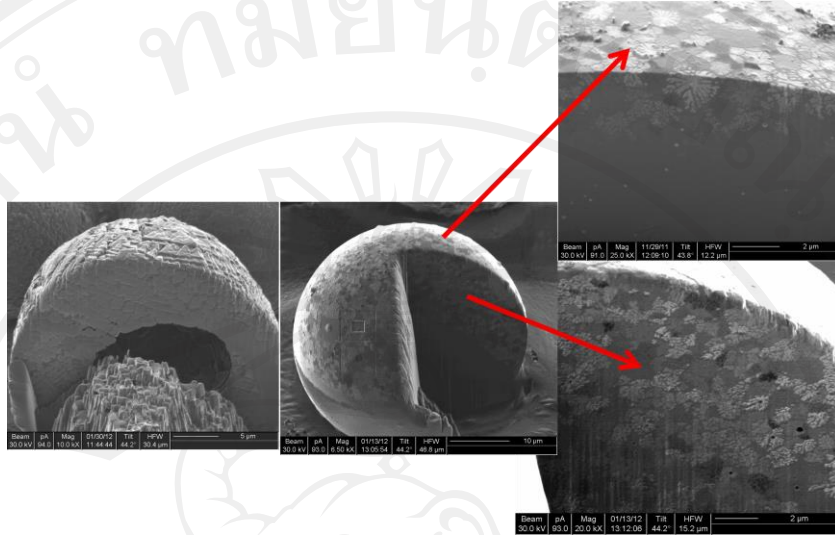


Figure 4.51 FIB images of pore and solid in-flight particles.

4.4 Characteristic of splats

Characteristics of all type of splat were studied including: WC-Cr-Ni, WC-Cr-Fe, and W-Cr-Fe nanocomposite. Details are described below.

4.4.1 Splat from WC-Cr-Ni cored wire

Splat particle from WC-Cr-Ni cored wire has disc shape produced from fully melted droplet as shown in Fig. 4.52.

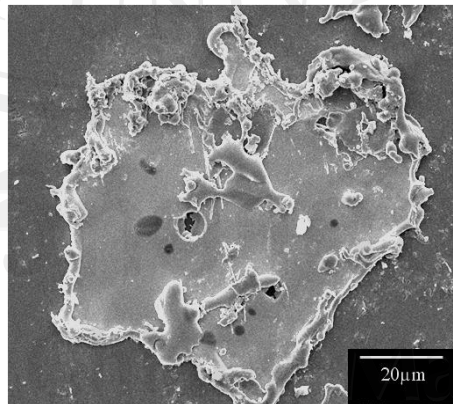


Figure 4.52 SE-SEM micrograph of disc shape WC-Cr-Ni splat.

Chemical composition of splat analysis by using EDS-SEM technique (Fig. 4.53) showed W, Ni, Cr, and C as major phases (Table 13).

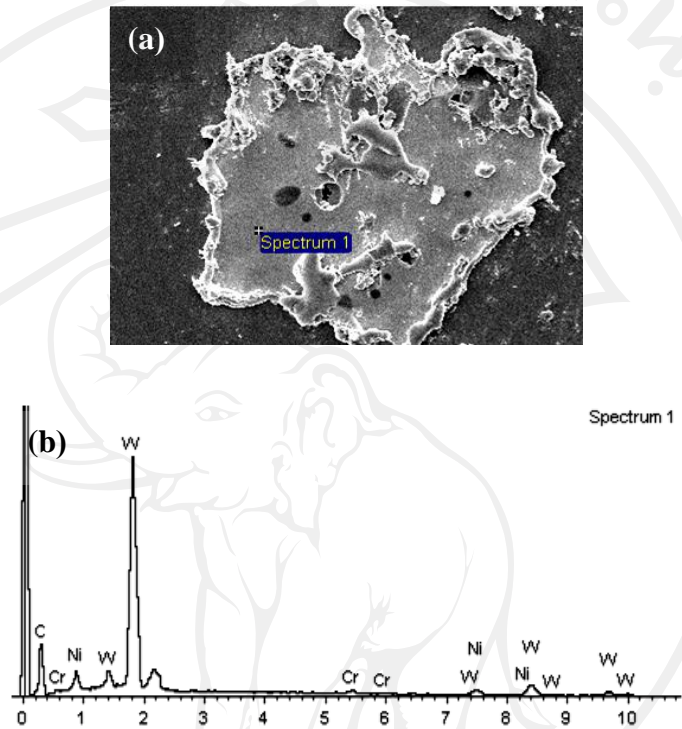


Figure 4.53 SEM micrograph of disc shape WC-Cr-Ni splat and (b) EDS spectrum.

Table 4.13 Chemical composition of WC-Cr-Ni splat.

| Element | W | Ni | Cr | C |
|---------|------|------|-----|------|
| wt% | 33.7 | 32.7 | 8.6 | 25.0 |

4.4.2 Splat from WC-Cr-Fe cored wire

Splat produced from WC-Cr-Fe cored wires (Fig. 4.54) (a) showed flower shape. Some particles form contiguous shape due to high cooling before impact as shown in Fig.

4.54 (b).

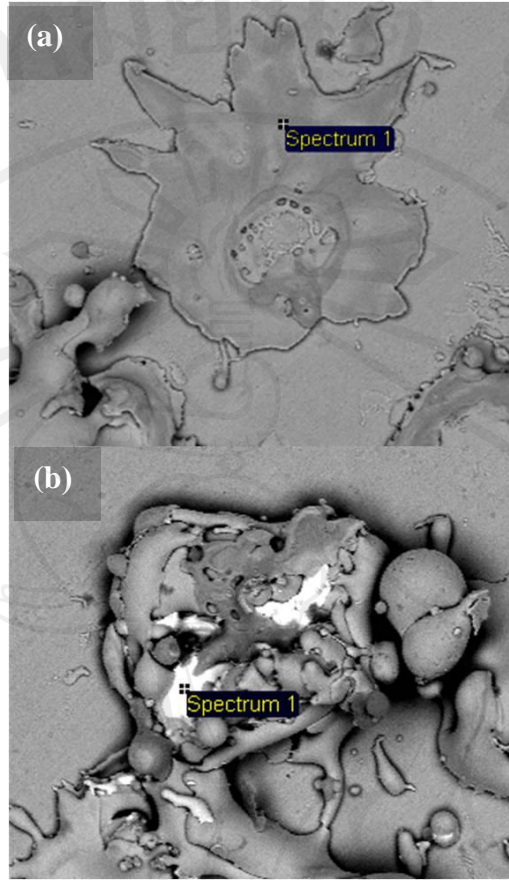


Figure 4.54 SE-SEM micrographs of flower and contiguous shape WC-Cr-Fe splat.

Chemical composition analysis of WC-Cr-Fe splat by using EDS-SEM technique were shown in Fig. 4.55 and 4.56. Chemical compositions is presented in Table 4.14.

Table 4.14 Chemical composition of WC-Cr-Fe splat.

| Element | Fe | W | Cr | Ni | C | O |
|------------|------|------|------|-----|------|------|
| Flower | 39.5 | | 23.8 | 3.3 | 16.4 | 17.1 |
| Contiguous | 23.6 | 55.5 | 3.3 | | 17.6 | |

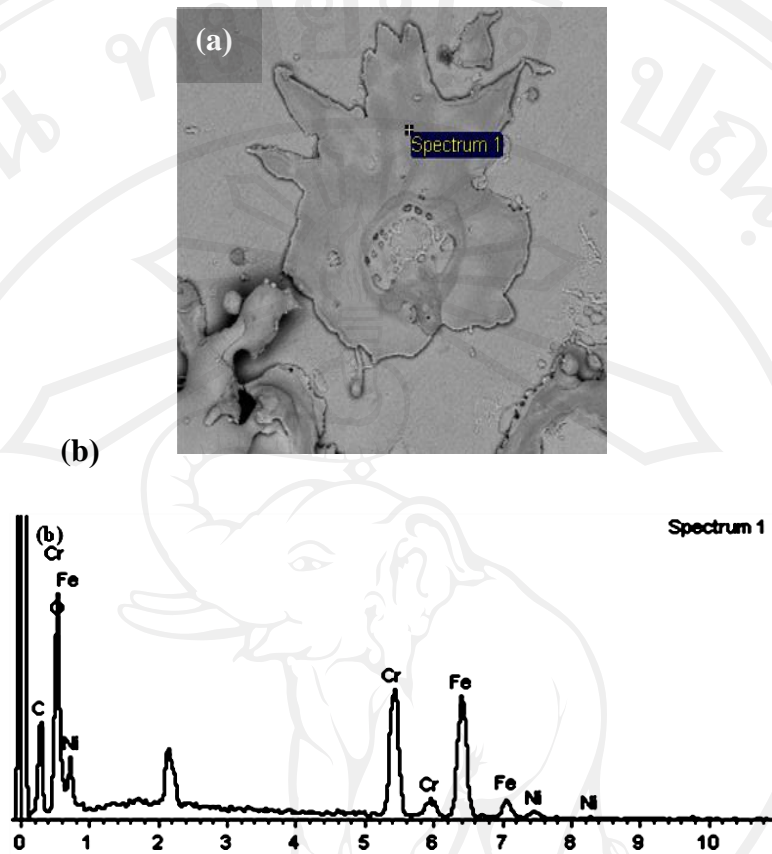


Figure 4.55 (a) SEM micrograph of flower shape WC-Cr-Fe splat and (b) EDS spectrum.

4.4.3 Splat from W-Cr-Fe nanocomposite cored wire

Splat from W-Cr-Fe nanocomposite cored wire showed a disc shape as shown in Fig. 4.57. EDS-SEM spectrum is shown in Fig. 4.58 with chemical compositions presented in Table 4.15.

Table 4.15 Chemical composition of W-Cr-Fe nanocomposite splat.

| Element | Fe | W | Cr | C | O |
|---------|------|-----|------|-----|-----|
| wt% | 70.4 | 5.3 | 19.7 | 3.4 | 1.1 |

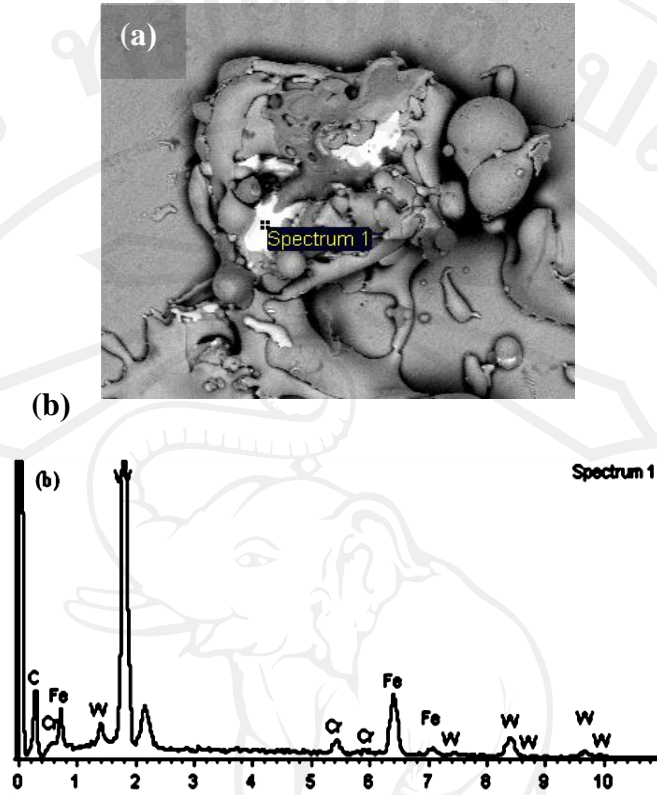


Figure 4.56 (a) SEM micrograph of contiguous shape WC-Cr-Fe splat and (b) EDS spectrum.

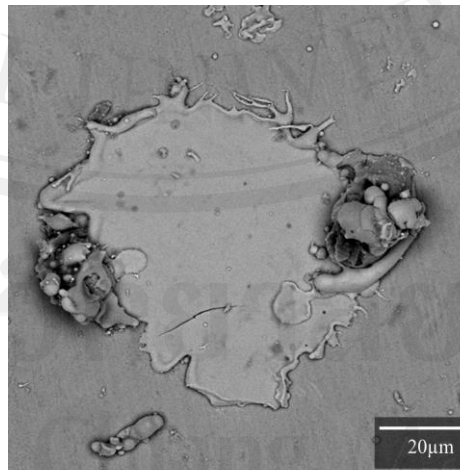


Figure 4.57 SE-SEM micrograph of a disc shape W-Cr-Fe nanocomposite splat.

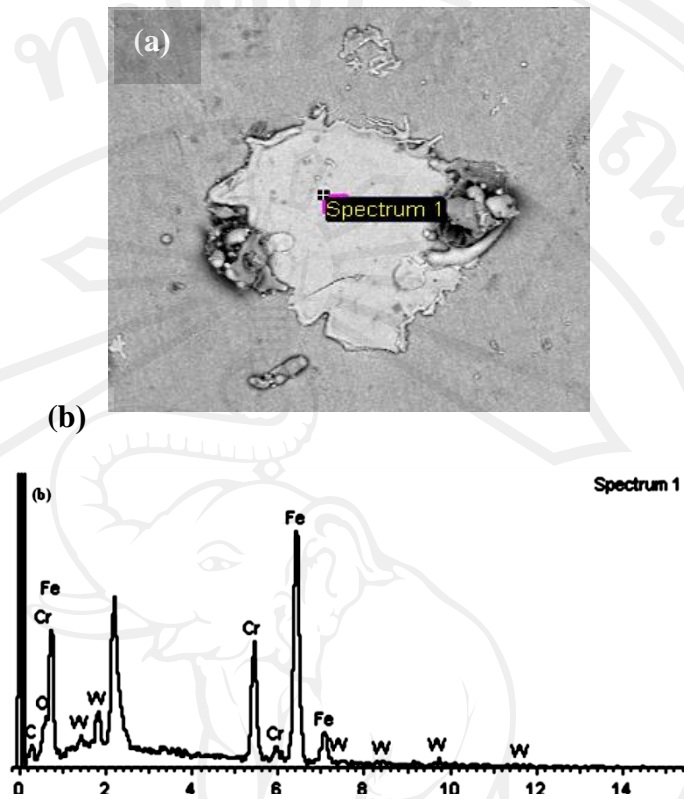


Figure 4.58 (a) SEM micrograph of a disc shape W-Cr-Fe nanocomposite splat and (b) EDS spectrum.

4.4.3 Summary of splat characteristics

Splat collection was done by spraying onto a polished stainless steel plate. Analysis by FIB showed typical void inside splat structure as shown in Fig.59. Splat morphology was revealed by OM and SEM technique. The typical shape of splat obtained by different core wire types are as follows: disc shape for WC-Cr-Ni splat, irregular and contiguous disc shape for WC-Cr-Fe splat, fragmented and flower shape for W-Cr-Fe nanocomposite splat. Splat sizes for all spray materials were calculated by using equation (3.2). The splat mean size, degree of flattening and degree of splashing (Table 15) were calculated by using

equation (3.2), (3.3) and (3.4) respectively. It is clearly seen that W-Cr-Fe nanocomposite wire had larger size of in-flight particle and also had a larger splat size, while the other two showed similar splat sizes. It should be noted that the disc shape like WC-Cr-Ni splat showed the highest degree of flattening (5.9) with the lowest degree of splashing (1.9), implying well spread of high viscous droplet. On the other hand, the W-Cr-Fe nanocomposite splat had the lowest degree of flattening (3.8) with the highest degree of splashing (3.3), and this means that most droplets (less viscous) had more splashing occurring on impact than spreading due to completely melted of shell and filler of the core wire. Splat characteristics of the WC-Cr-Fe splat were in between the other two as displayed in the table 4.16

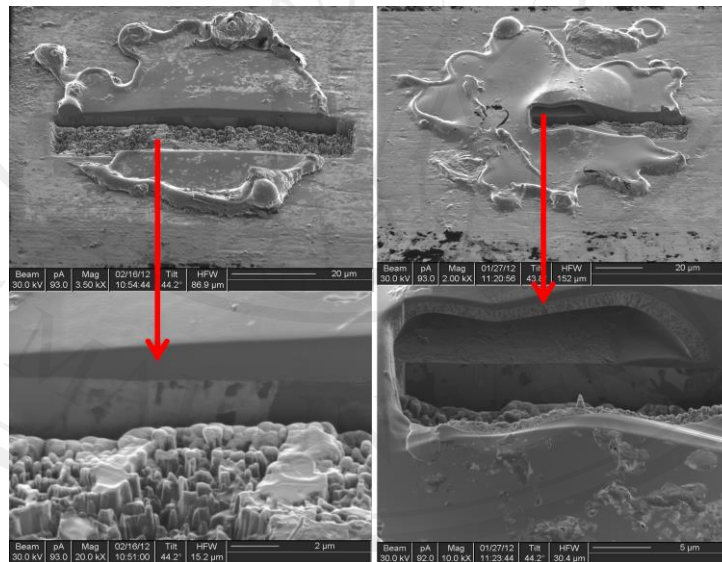


Figure 4.59 FIB micrographs showing solid and pore splat.

Table 4.16 Characteristics of in-flight particle and splat.

| Type of particle | Mean size (μm) | | | Degree of flattening | Degree of splashing |
|-----------------------|-----------------------------|--------------------|-------|----------------------|---------------------|
| | filler particle | in-flight particle | splat | | |
| WC-Cr-Ni | 40 | 12 | 71 | 5.9 | 1.9 |
| WC-Cr-Fe | 53 | 18 | 70 | 3.9 | 2.5 |
| W-Cr-Fe nanocomposite | 52 | 26 | 100 | 3.8 | 3.3 |

4.5 Characteristics of coating

Characterization of all coatings including 86WC-4Cr-10Co, WC-Cr-Ni, WC-Cr-Fe, and W-Cr-Fe nanocomposite coating were detailed in the following sections which included roughness, thickness, microstructure, chemical compositions, porosity, hardness, phase compositions, sliding and abrasive wear rate.

4.5.1 Roughness

Roughness of all types of coating was tested by roughness analyzer. It was found that 86WC-4Cr-10Co coating had the lowest roughness ($6.1 \mu\text{m}$) compared to others coating. It could be as a result of a high velocity of particle on impact produce by HVOF technique. However, comparison within a group of arc sprayed coatings, it was found that W-Cr-Fe nanocomposite coating showed the lowest roughness value $13.7 \mu\text{m}$ of the group as shown in Table 4.17. This could be due to fully melted of W-Cr-Fe nanocomposite cored wires filler that can be seen in Fig. 4.52.

Table 4.17 Characteristic of coatings.

| Coating | Characteristics | | | |
|--------------------------|--------------------------------|--------------------------------|-----------------|-----------------------------------|
| | Thickness (μm) | Roughness (μm) | Porosity (%) | Hardness (HV _{300g}) |
| 86WC-4Cr-10Co | 450 | 6.1 \pm 0.6 | 1.5 \pm 0.9 | 1178 \pm 162 |
| WC-Cr-Ni | 500 | 15.8 \pm 1.7 | 8.0 \pm 1.3 | 1034 \pm 202 |
| WC-Cr-Fe | 500 | 16.3 \pm 1.6 | 9.2 \pm 1.6 | 802 \pm 144 |
| W-Cr-Fe nanocomposite | 500 | 13.7 \pm 1.1 | 4.8 \pm 1.7 | 1094 \pm 82 |

4.5.2 Thickness

Thickness of coating from HVOF and arc spraying are specified as 450 μm and 500 μm , respectively. Measurement of thickness of coating with SCENTIS analysis software revealed that 86WC-4Cr-10Co coating had a thickness of about 450 μm , while WC-Cr-Ni, WC-Cr-Fe, and W-Cr-Fe nanocomposite coatings had thickness of about 500 μm , as shown in Table 4.17.

4.5.3 Microstructure

4.5.3.1 86WC-4Cr-10Co coating

Microstructure of HVOF sprayed 86WC-4Cr-10Co coating revealed by SEM was very dense structure (Fig. 4.60). High velocity particles generated by HVOF spraying resulted in a strong cohesion. The interface between the coating and substrate was very well bonded as shown in Fig. 4.60 (e).

4.5.3.2 WC-Cr-Ni coating

Fig. 4.61 shows microstructure of WC-Cr-Ni coating in which coating contained splat structure, pores and unmelted particles dispersion in the coating. Multi phase structure

was also clearly seen from different contrast shown in Fig 4.61 implying different phase compositions in the containing.

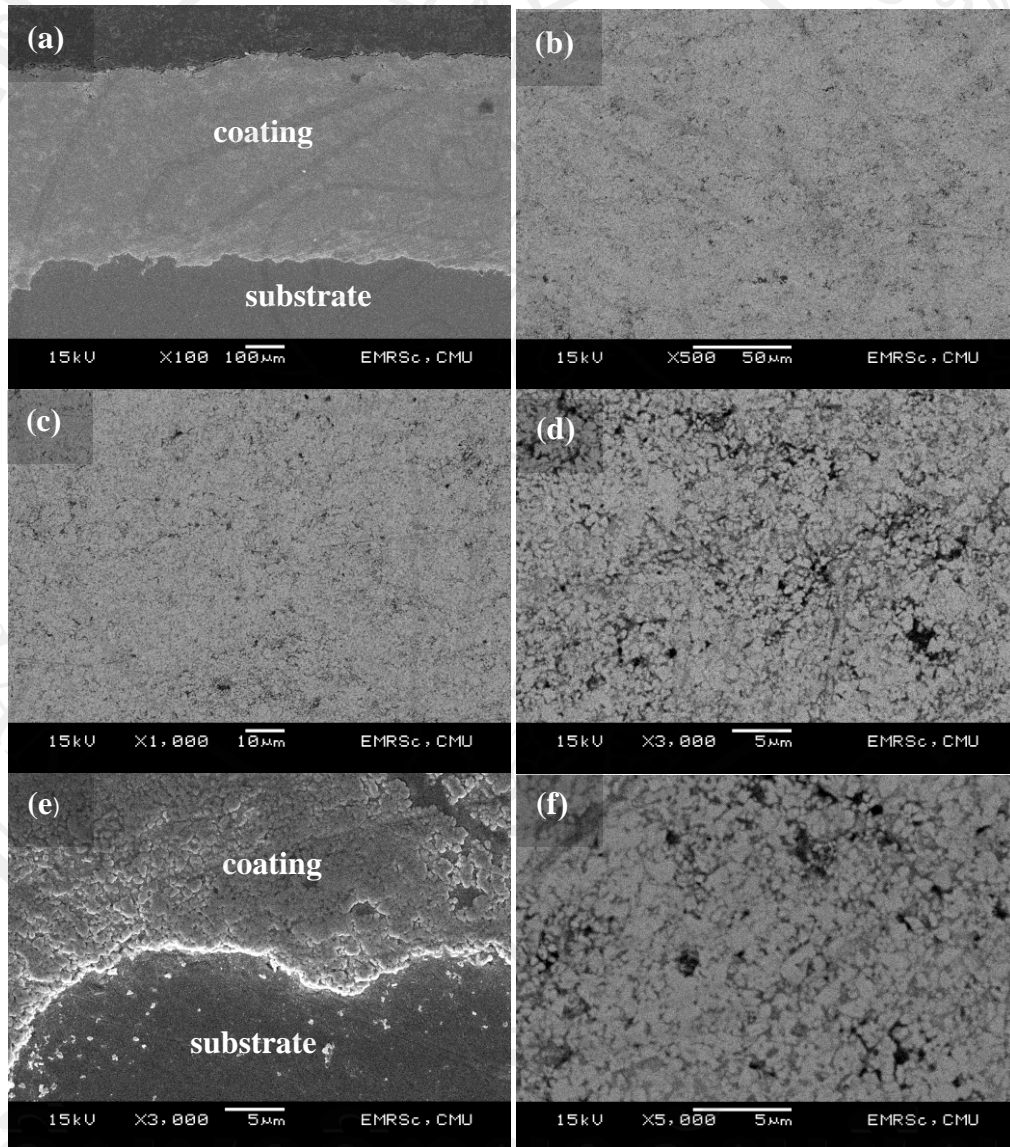


Figure 4.60 BSE-SEM micrographs of 86WC-4Cr-10Co coating; (a) 100X, (b) 500X, (c) 1000X, (d) 3000X, (e) 3500X at the interface, and (f) 5000X.

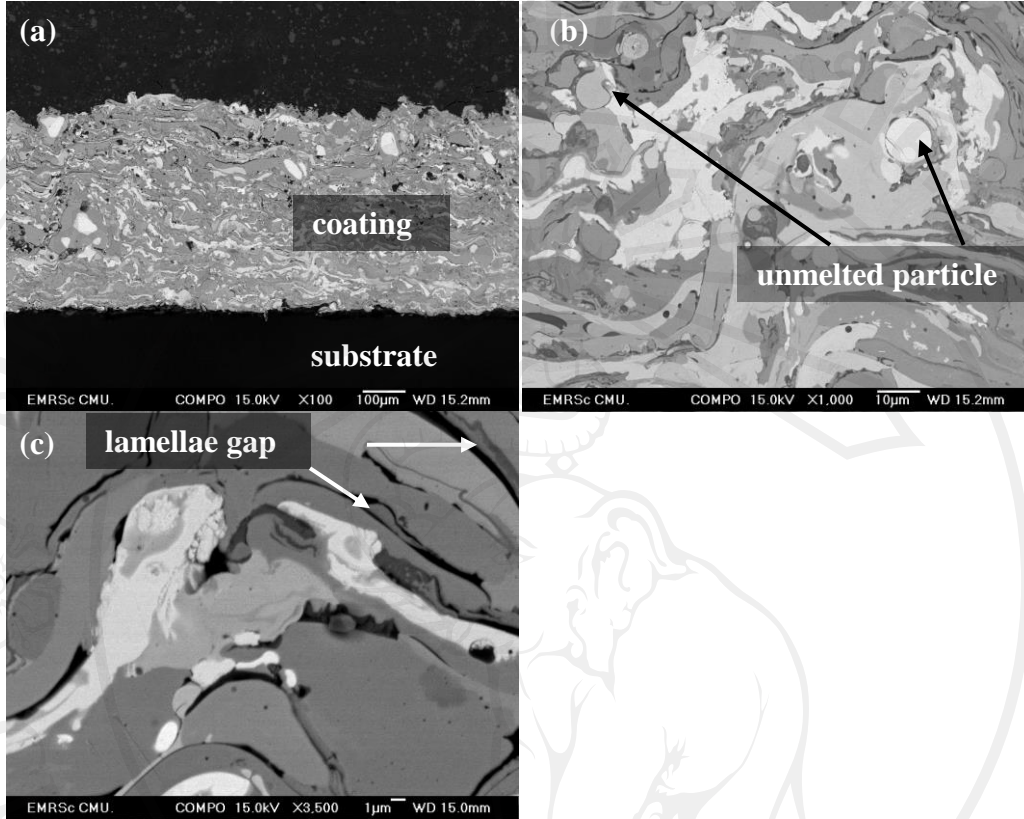


Figure 4.61 BSE-SEM micrographs show cross-sections of WC-Cr-Ni coating at a 100X, (b) 1000X, and (c) 3500X.

4.5.3.3 WC-Cr-Fe coating

Fig. 4.62 shows SEM micrograph of WC-Cr-Fe coating at difference magnifications. It is clearly seen that the structure of the coating were splat like structure.

At high magnification it can be seen that the gap at interface was narrower than WC-Cr-Ni coating indicating better melting. Splat in the coating had various phase compositions.

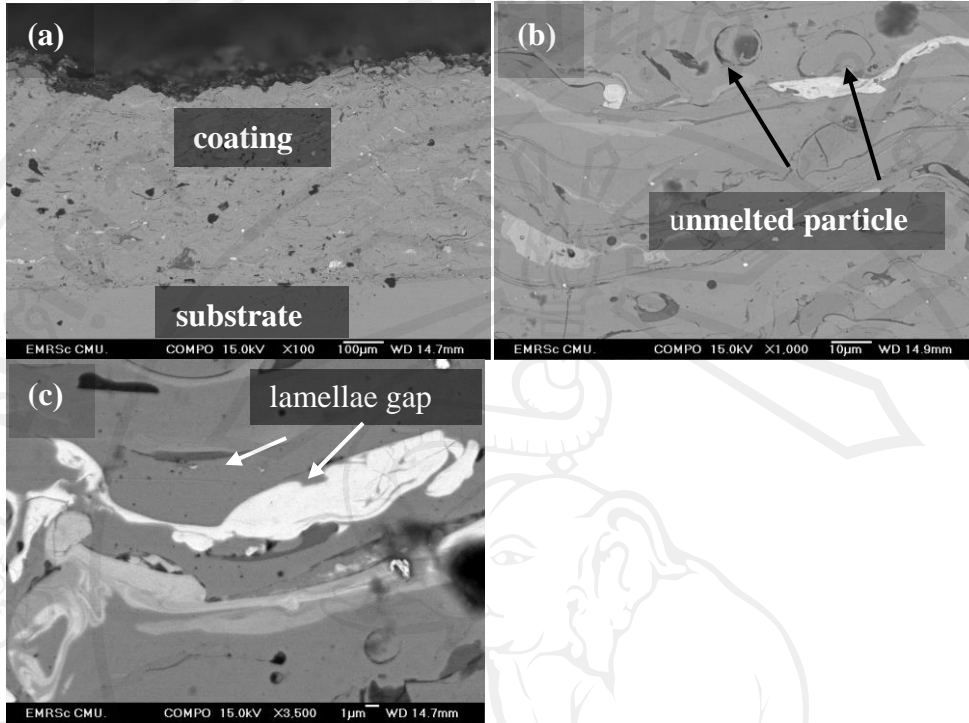


Figure 4.62 BSE-SEM micrograph show cross-sections of WC-Cr-Fe coating at (a) 100X, (b) 1000X, and (c) 3500X magnification.

4.5.3.4 W-Cr-Fe nanocomposite coating

Microstructure of W-Cr-Fe nanocomposite coating revealed by scanning electron microscope was shown in Fig. 4.63. The coating consisted a multi layered structure. At high magnification the interface between splat were narrower than the WC-Cr-Ni and WC-Cr-Fe coatings implying good cohesion from well melted particles.

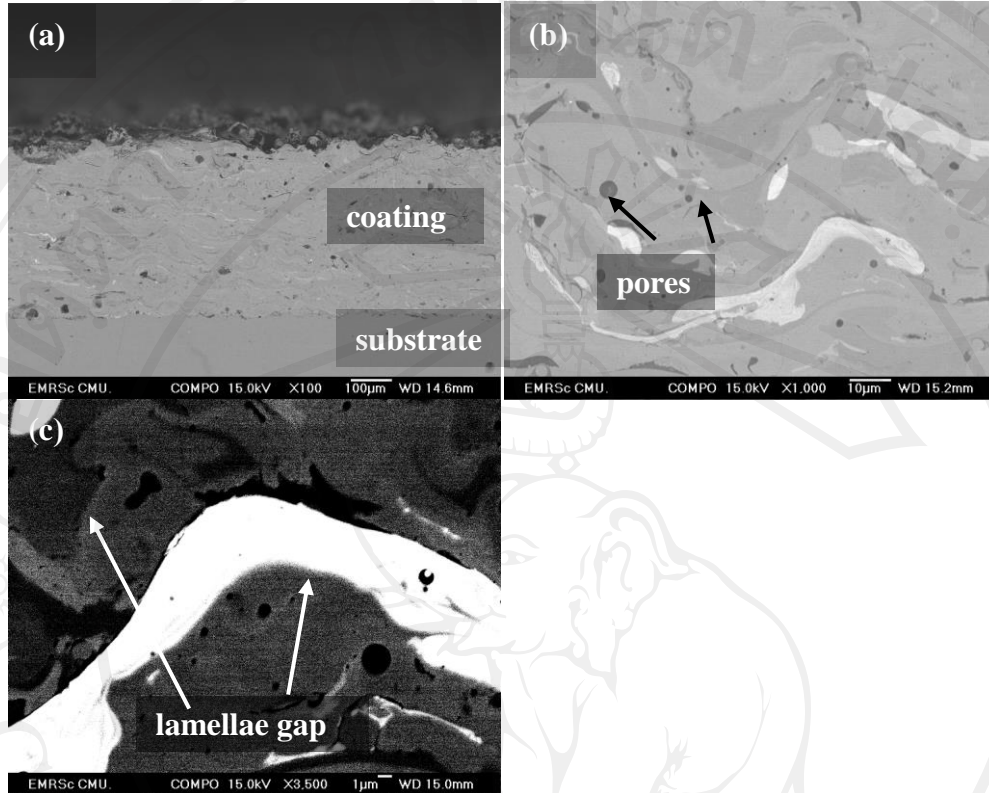


Figure 4.63 BSE-SEM micrographs show cross-section of W-Cr-Fe nanocomposite coating at (a) 100X, (b) 1000X, and (c) 3500X.

4.5.4 Chemical Compositions

4.5.4.1 86WC-4Cr-10Co coating

Chemical compositions of the coating analyzed by EDS-SEM was found to be W, C, Cr, and Co as principle components with W up to 82 wt%. Chemical composition was presented in Table 4.18. Spectrum of the 84WC-4Cr-10Co coating from EDS analysis was shown in Fig. 4.64.

Table 4.18 Chemical composition of 86WC-4Cr-10Co coating.

| Element | wt% | at% |
|---------|------|------|
| W | 82.2 | 32.5 |
| C | 9.4 | 56.6 |
| Cr | 3.2 | 4.5 |
| Co | 5.2 | 6.4 |

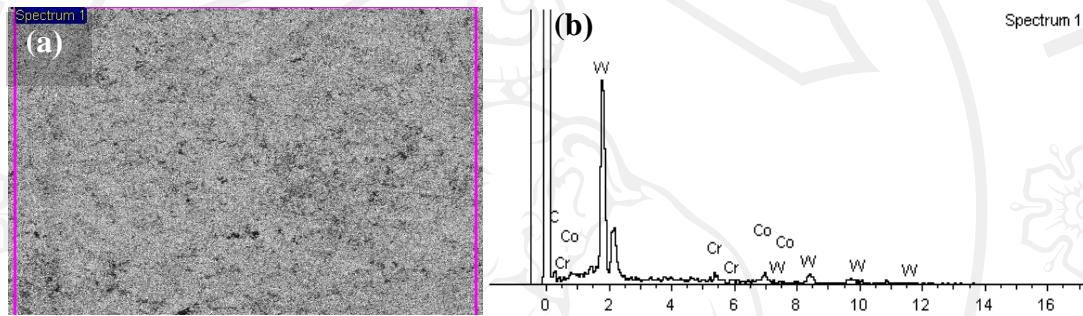


Figure 4.64 (a) SEM micrograph of 86WC-4Cr-10Co coating and (b) EDS spectrum.

4.5.4.2 WC-Cr-Ni coating

Chemical composition of the WC-Cr-Ni coating analyzed by EDS-SEM (area analysis) was shown in the table 4.19 with W, Ni, Cr, C, and O as major components. EDS spectrums of the coating was shown in Figure 4.65. EDS spot analysis of the bright area was found to be W at 84.5 wt% with some Ni, Cr and others as shown in Table 4.20. EDS spectrum of the bright area taken from Fig. 4.66 indicated that this area was mainly composed of W.

Table 4.19 Chemical compositions of WC-Cr-Ni coating by area analysis.

| Element | wt% | at% |
|---------|------|------|
| W | 50.0 | 15.5 |
| Ni | 34.7 | 35.9 |
| Cr | 10.2 | 11.9 |
| C | 4.4 | 22.2 |
| O | 3.8 | 14.5 |

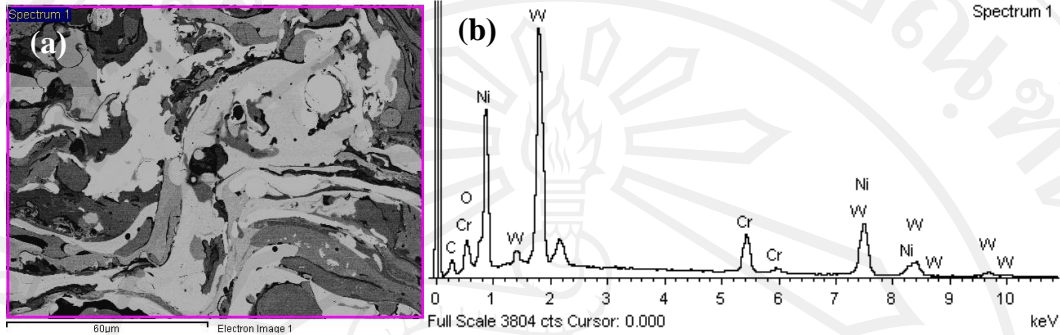


Figure 4.65 (a) BSE-SEM micrographs of WC-Cr-Ni coating and (b) EDS spectrum of area analysis.

Table 4.20 Chemical compositions of WC-Cr-Ni coating by point analysis.

| Element | wt% | at% |
|---------|------|------|
| W | 84.5 | 45.0 |
| Ni | 8.8 | 14.7 |
| Cr | 2.3 | 4.4 |
| C | 4.4 | 36.0 |

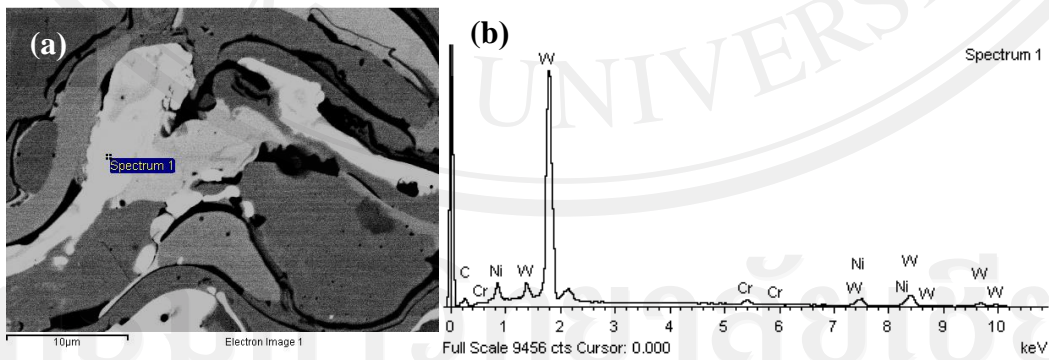


Figure 4.66 (a) SEM micrograph of WC-Cr-Ni coating and (b) spectrum EDS of point analysis.

4.5.4.3 WC-Cr-Fe coating

Chemical analysis of the WC-Cr-Fe coating by EDS-SEM technique found that Fe, Cr, Ni, W, C and O as major components with the highest content of Fe. (Table 4.21) EDS spectrum was shown in Fig. 4.67. The bright area was composed of W, Cr, Fe and C, as shown in Table 4.22. EDS spectrum of the bright area was shown in Fig. 4.68.

Table 4.21 Chemical composition of WC-Cr-Fe coating by area analysis.

| Element | wt% | at% |
|---------|------|------|
| Fe | 67.3 | 56.7 |
| Cr | 14.0 | 12.7 |
| Ni | 6.6 | 5.2 |
| W | 5.3 | 1.4 |
| C | 4.0 | 15.6 |
| O | 3.0 | 15.6 |

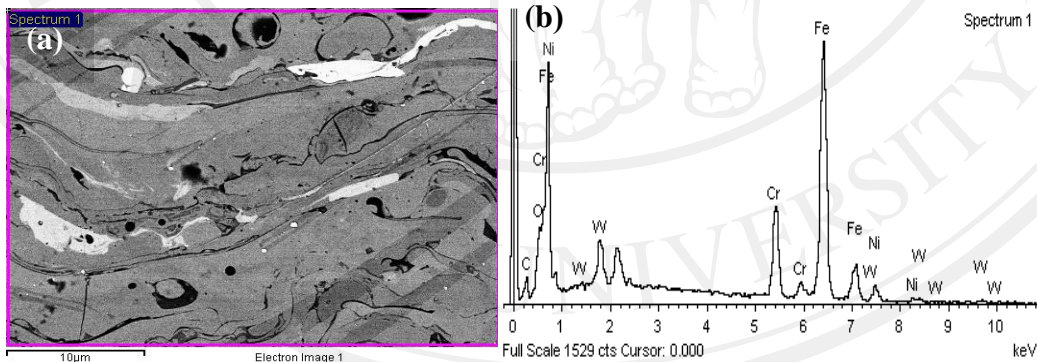
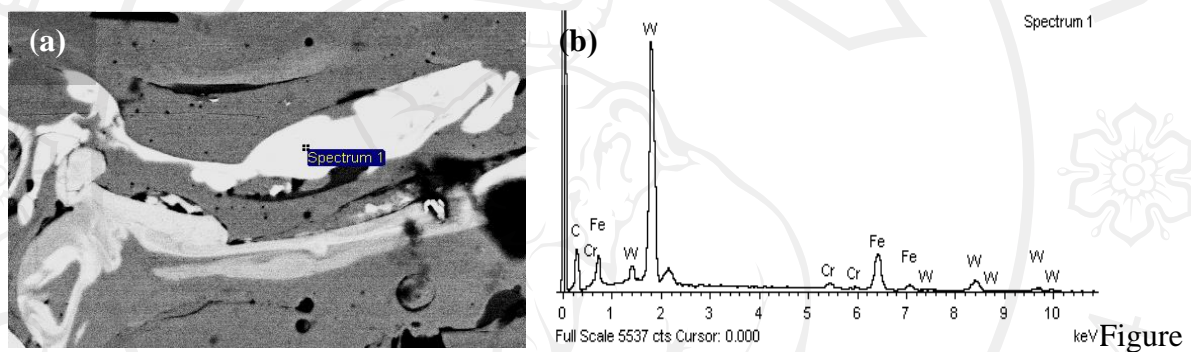


Figure 4.67 (a) BSE-SEM micrograph of WC-Cr-Fe coating and (b) EDS spectrum of area analysis.

Table 4.22 Chemical composition of WC-Cr-Fe coating by point analysis.

| Element | wt% | at% |
|---------|------|------|
| W | 60.0 | 15.2 |
| Fe | 21.2 | 17.6 |
| Cr | 2.0 | 1.7 |
| C | 17.0 | 65.5 |



4.68 (a) SEM micrograph of WC-Cr-Fe coating and (b) EDS spectrum of point analysis.

4.5.4.4 W-Cr-Fe nanocomposite coating.

Chemical compositions of the W-Cr-Fe nanocomposite coating analyzed by EDS-SEM technique showed Fe as main components (at 58.1 wt%). Other chemical compositions were presented in Table 4.23. EDS spectrum was shown in Fig. 4.69. Spot analysis of the bright area showed W as main component (at 62.3 wt%) as shown in Table 4.24. EDS spectrum of the bright area from spotted EDS was shown in Fig. 4.70.

Table 4.23 Chemical composition of W-Cr-Fe nanocomposite coating by area analysis.

| Element | wt% | at% |
|---------|------|------|
| Fe | 58.3 | 53.1 |
| Cr | 15.6 | 15.2 |
| Nb | 10.7 | 5.7 |
| W | 9.3 | 2.6 |
| C | 3.7 | 15.5 |
| O | 2.5 | 7.8 |

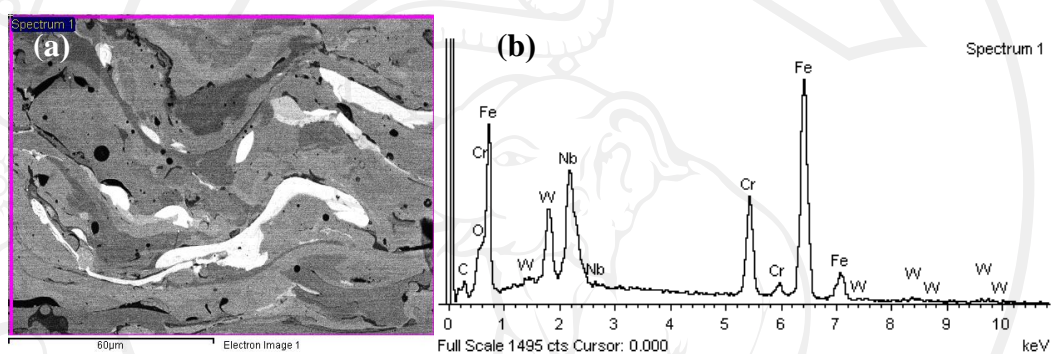


Figure 4.69 (a) BSE-SEM micrograph of W-Cr-Fe nanocomposite coating and (b) EDS-spectrum of area analysis.

Table 4.24 Chemical composition of W-Cr-Fe nanocomposite coating.

| Element | wt% | at% |
|---------|------|------|
| W | 62.3 | 28.7 |
| Fe | 28.7 | 43.4 |
| Cr | 6.7 | 10.9 |
| C | 2.4 | 17.0 |

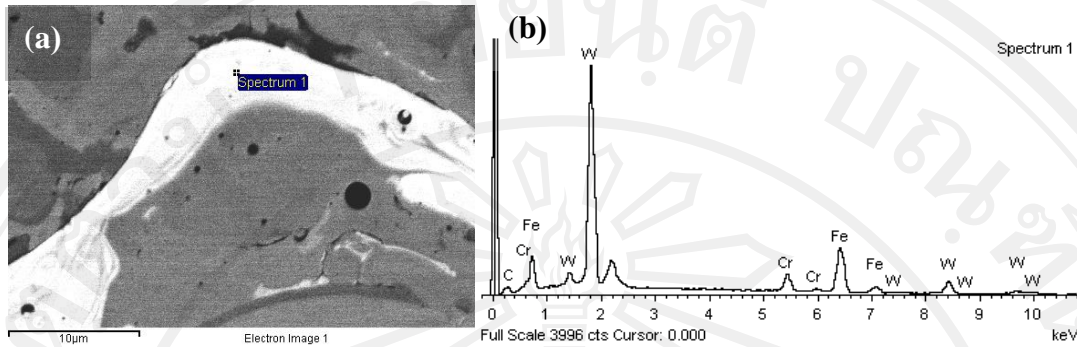


Figure 4.70 (a) BSE-SEM micrograph of W-Cr-Fe nanocomposite coating and (b) EDS spectrum of point analysis.

4.5.5 Porosity

Porosity of all types of coating was evaluated by SCENTIS image analysis technique. It was found that 86WC-4Cr-10Co coating had the lowest porosity (1.5%). It is as a result of high density coating microstructure produced by HVOF spraying. Comparison within a group of arc spray coating, it was found that W-Cr-Fe nanocomposite coating had the lowest porosity at 4.8 percent (Table 4.17). This could be due to the nanostructure of the fillers. WC-Cr-Fe cored wires had the highest amount of porosity at 9.2 percent due to incomplete melting of the cored wire fillers.

4.5.6 Hardness

Coating microhardness was measured by Vicker's micro hardness tester with 300 g load 5 seconds dwell time. The average hardness value of 86WC-4Cr-10Co, WC-Cr-Ni, WC-Cr-Fe, and W-Cr-Fe nanocomposite cored wires were 1178 HV_{300g}, 1034 HV_{300g}, 802 HV_{300g}, and 1094 HV_{300g}, respectively (Table 4.25). The 86WC-4Cr-10Co coating had the

highest hardness because of its high density and lower porosity. Moreover, it also contained a high amount of cermet materials (WC). In a group of arc sprayed coating W-Cr-Fe nanocomposite coating had the highest hardness, due to its high density and low porosity. The hardness of WC-Cr-Ni coating was nearly as high as that of the W-Cr-Fe nanocomposite coating (1034 HV_{300g}) because it had high amount of cermet material content.

4.5.7 Phase Compositions

4.5.7.1 WC-Cr-Ni coating

Analysis of phase compositions of WC-Cr-Ni coating using XRD technique showed WC, W₂C and Ni as main components at 29.53, 3.39 and 67.08 percent of phase contain respectively. X-ray diffraction patterns was shown in Fig. 4.71.

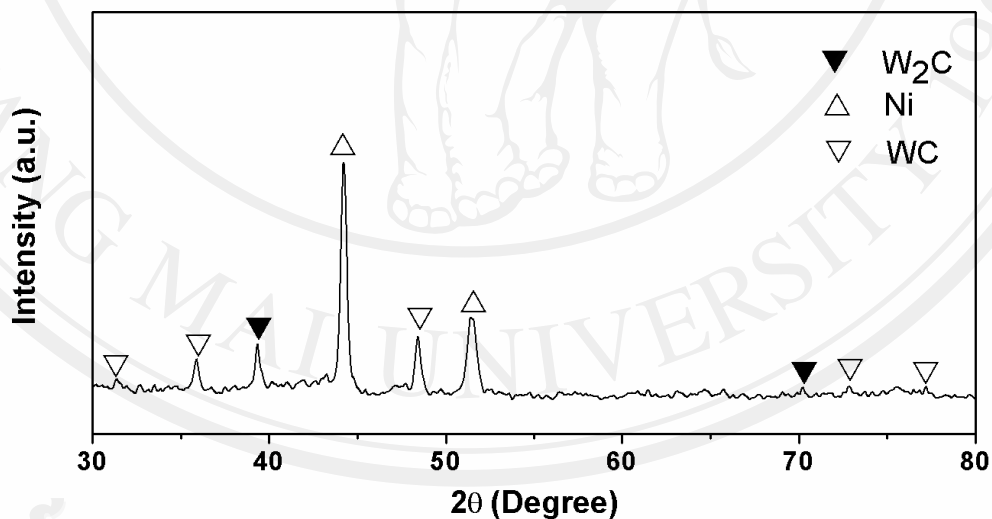


Figure 4.71 X-ray diffraction patterns of WC-Cr-Ni coating.

4.5.7.2 WC-Cr-Fe coating

Fig. 4.72 shows X-ray diffraction patterns of WC-Cr-Fe coating which consisted of FeC, Fe, WC, W₂C, and Cr as 4.34, 13.85, 29.91, 20.06 and 31.84 percent of phase contain respectively.

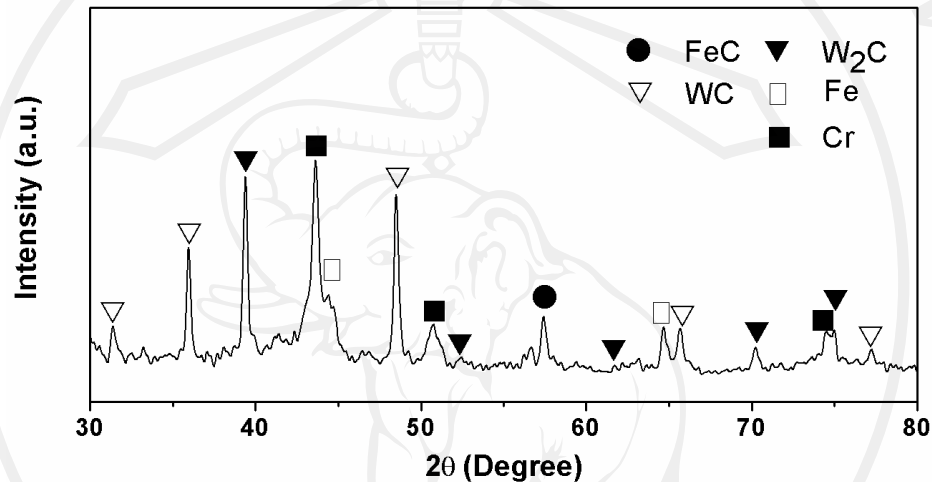


Figure 4.72 X-ray diffraction patterns of WC-Cr-Fe coating.

4.5.7.3 W-Cr-Fe nanocomposite coating

Analysis of phase compositions of W-Cr-Fe nanocomposite coating using X-ray diffraction analyzer showed FeC, Fe, WC, W₂C and Cr as main components at 3.17, 29.46, 20.43, 26.91 and 20.03 percent of phase contain respectively X-ray diffraction pattern was shown in Fig. 4.73.

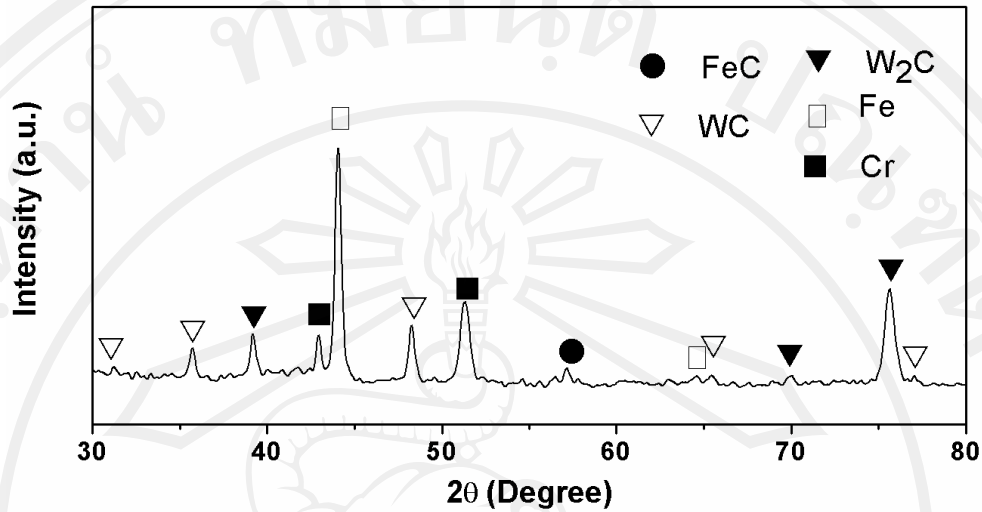


Figure 4.73 X-ray diffraction patterns of W-Cr-Fe nanocomposite coating.

4.5.8 Summary of coating characteristics

Microstructures of the arc sprayed cored-wire coatings were revealed by BSE-SEM micrographs of coating cross-sections as shown in Fig. 4.74. Complex structures that composed of multi-phase are typically found in WC-M sprayed coatings Fig. 4.74 (a-c) show the microstructure of WC-Cr-Ni coating which exhibited a “splat-like” complex structure as various contrast were observed. This coating had less dense structure compared to the others. The un-melted and semi-molten particles with irregular shape were widely observed in the coating. Oxides with some voids and cracks along splat boundaries were clearly seen. Various contrasts implied a multi-phase present as result of phase transformation during spray process. Fig. 4.74 (c1) shows W-rich (very bright contrast) and Ni-rich phase that clearly identified by EDS-SEM shown in Fig.4.74 (c2). High content of hard carbide phase from starting cored-wire could contribute to a less dense structure of coating obtained; however, this raised the coating hardness. In addition, the more carbide

content would lead to the more decarburization resulted in phase transformation as given by equation (4.1) [32, 34-35]. WC, W₂C and Ni were major phases found in the coating by XRD analysis (Fig. 75a)



WC-Cr-Fe coating exhibited lamellar, dense and homogeneous structure. W-rich was observed as very bright regions and Fe-Ni-Cr-rich as gray regions shown in Fig. 4.74 (e-f) which identified by EDS-SEM. The hardness evaluation of this coating showed the lowest value of the three cored wires, due to its high content of metallic binder phase. Porosity and denseness of coating were comparable to that of the WC-Cr-Ni coating. Phase transformation was also observed as identified by the XRD pattern shown in Fig. 75(b). The presence of prominent peaks of WC, W₂C and FeC along with Fe and Cr peaks was clearly indexed. W-Cr-Fe nanocomposite coating had a smooth surface, very dense structure and low porosity compared to others. Fig. 4.74(g-i) shows fine-structured splat with excellent cohesion found in this coating. Lamella splats with very dense structure implied the predominant in-flight particles that being fully molten or semi-molten on impact. Chemical analysis by EDS-SEM revealed W-rich phase as bright regions and Fe-Ni-Cr-rich as gray regions depicted in Fig.4.74(i). XRD pattern showed principal phases in the coating as WC, W₂C, FeC, Fe and Cr. (Fig. 4.75c)

In addition, characteristics of the in-flight particle detailed in previous work can be correlated with coating characteristics [17]. The mean sizes of in-flight particles measured by laser diffraction technique were 12 μm for WC-Cr-Ni, 18 μm for WC-Cr-Fe and 26 μm

for W-Cr-Fe nanocomposite. It is likely that the more metallic phase (from metallic shell and filler) of the cored-wire, the larger size of in-flight particle produced. This demonstrates the role of the more easily melted metallic phase forming in-flight particles. The W-Cr-Fe nanocomposite wire, had a similar mean size of filler particle to that of WC-Cr-Fe wire, however, had more benefit of finer structure and more metallic content resulted in high homogeneity, well melted and larger mean size of in-flight particles. This led to well bonded splats and therefore, dense coating microstructure.

The superior coating hardness could be as a result of amorphous phase and nanostructured (Fig. 4.76). In W-Cr-Fe nanocomposite coating containing 12% niobium content. Niobium had high cooling rate during solidification. [46, 48, 49-54]

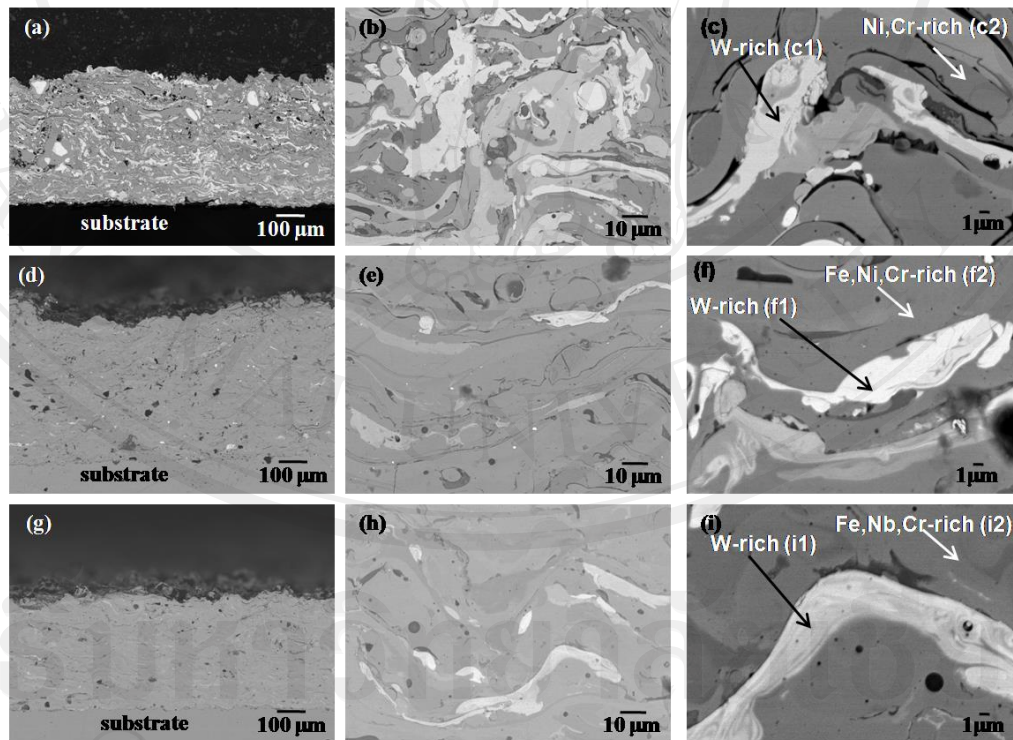


Figure 4.74 BSE-SEM micrographs illustrate coating microstructure at different magnifications: (a, b, c) WC-Cr-Ni; (d, e, f) WC-Cr-Fe; (g, h, i) W-Cr-Fe nanocomposite.

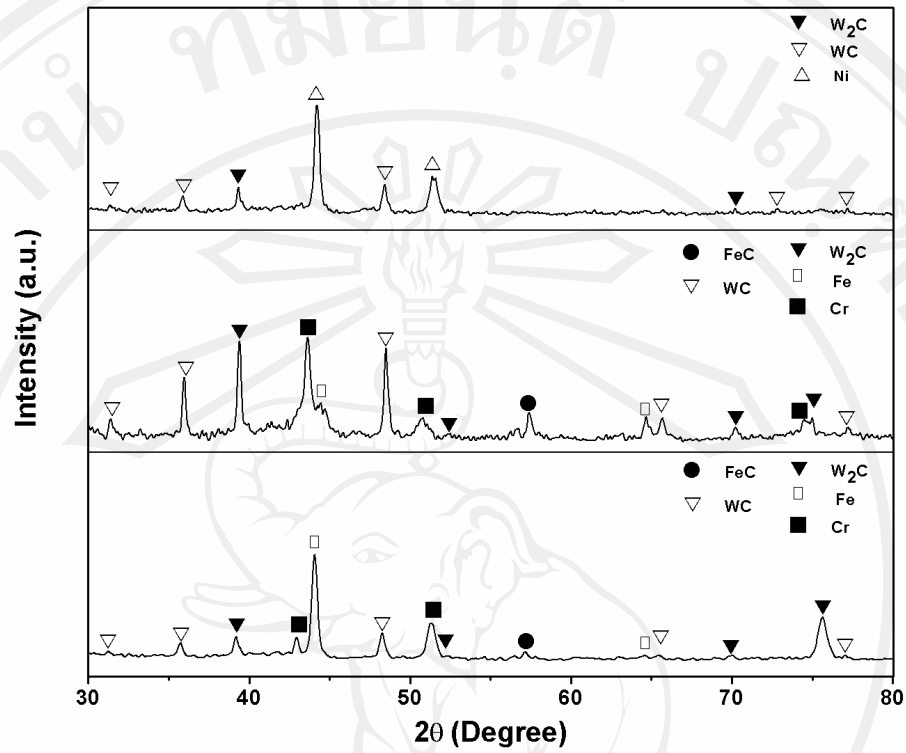


Figure 4.75 X-ray patterns of coatings : (a) WC-Cr-Ni; (b) WC-Cr-Fe; (c) W-Cr-Fe nanocomposite.

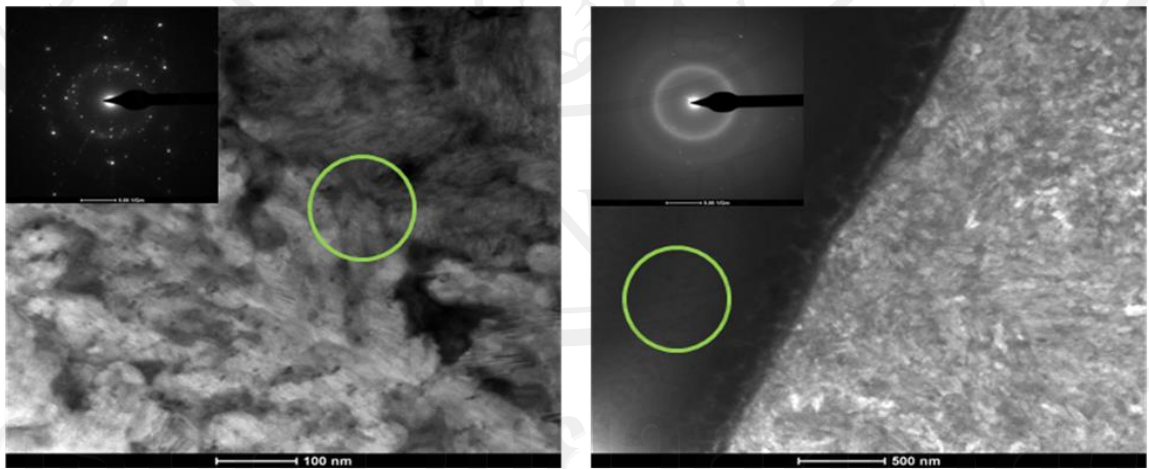


Figure 4.76 TEM-SADP micrographs showing amorphous and nanostructure of W-Cr-Fe nanocomposite coating.

4.6 Wear test of coatings

4.6.1 Sliding wear test

Sliding wear was tested by pin on disk tester (ISC-200 TRIBIMTER) using 3.15 mm-diameter WC-Co ball pressing head and the pressing weight of 1000 g. The distance was 500 m with linear velocity of 7.5 cm/min. Results of the test are described below.

4.6.1.1 WC-Cr-Ni coating

The WC-Cr-Ni coating had the lowest of wear rate of 0.0334 mg/m, (Table 4.25). This is from high WC in WC-Cr-Ni coating. The shallow wear tracks as well as untracked area were found as shown in Fig. 4.77.

Table 4.25 Sliding and abrasive wear of coating.

| Coating | Sliding wear (mm ³) | Abrasive wear (g/m) |
|-----------------------|------------------------------------|------------------------|
| 86WC-4Cr-10Co | - | 0.16 |
| WC-Cr-Ni | 0.0334 ±0.000 | 0.047 ±0.003 |
| WC-Cr-Fe | 0.0718 ±0.006 | 0.049 ±0.009 |
| W-Cr-Fe nanocomposite | 0.0610 ±0.006 | 0.041 ±0.005 |

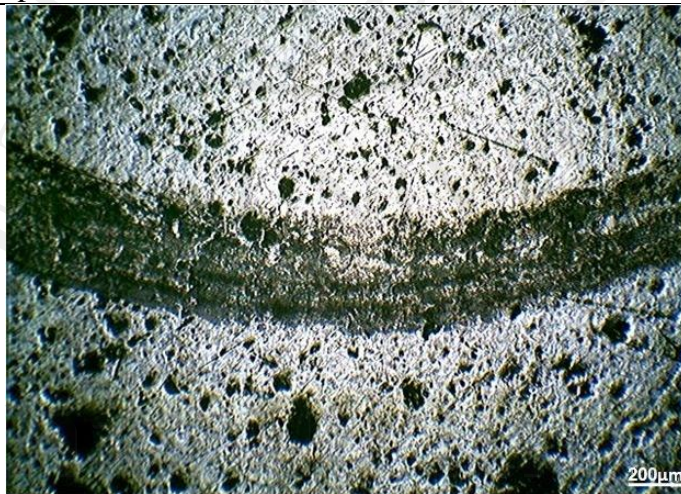


Figure 4.77 OM image showing wear track of WC-Cr-Ni coating at 100X magnification.

4.6.1.2 WC-Fe coating

The WC-Cr-Fe coating had the highest wear rate of 0.0718 mg/m, compared to WC-Cr-Ni and W-Cr-Fe nanocomposite coatings. This is because the WC-Cr-Fe coating has low hardness value and high porosity. Wear tracks were found to be wide and uneven as shown in Fig. 4.78.

4.6.1.3 W-Cr-Fe nanocomposite coating

The W-Cr-Fe nanocomposite coating had wear rate of 0.0610 mg/m. This is because the W-Cr-Fe nanocomposite coating has high density, low porosity and high hardness. Its wear track were shallow and even, as shown in Fig. 4.79



Figure 4.78 OM image shows wear track of WC-Cr-Fe coating at 100X magnification.

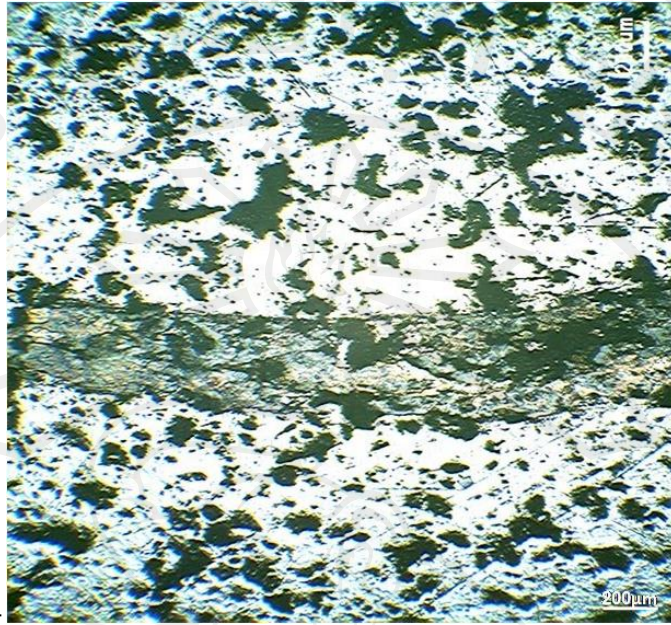


Figure 4.79 OM image shows wear track of W-Cr-Fe nanocomposite coating at 100X magnification.

4.6.2 Abrasive wear

Abrasive wear rate was tested with dry sand rubber wheel, according to ASTM G65 standard with 60 μm brown Al_2O_3 . Details of coating wear rate are discussed below.

4.6.2.1 86WC-4Cr-10Co coating

The 86WC-4Cr-10Co coating had the wear rate of 0.016 g/m as shown in Fig. 4.80 and table 4.24. This coating had highest wear resistance due to its high density. Analysis of worn surface showed shallow and shiny polished track, as shown in Fig. 4.81.

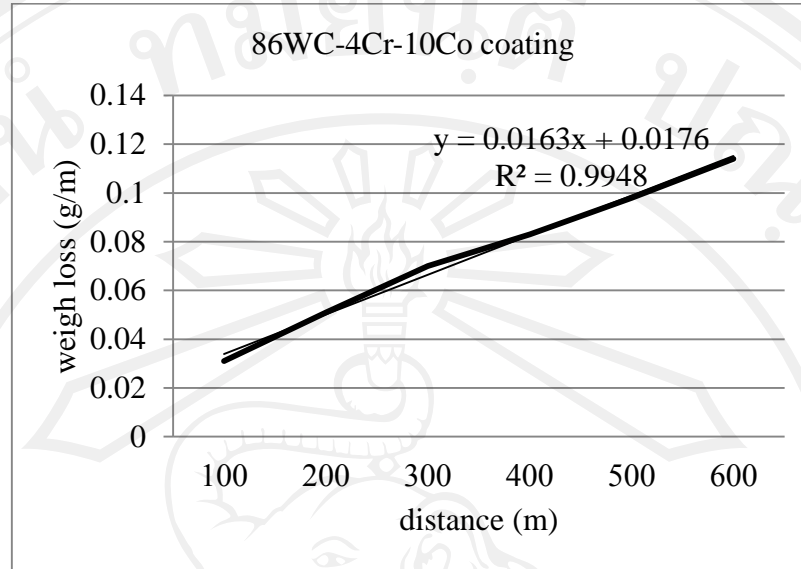


Figure 4.80 Abrasive wear rate of 86WC-4Cr-10Co coating.

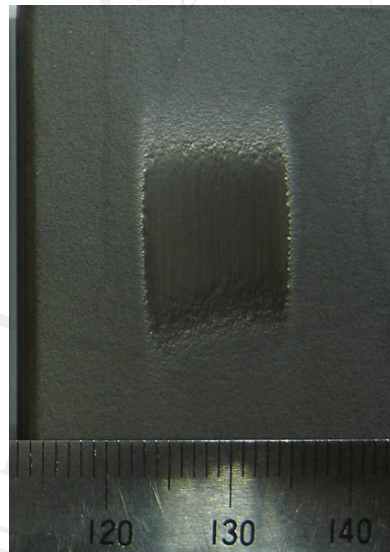


Figure 4.81 Worn surface of 86WC-4Cr-10Co coating following abrasive wear test.

4.6.2.2 WC-Cr-Ni coating

Abrasive wear rate of WC-Cr-Ni coating was 0.047 g/m (Fig. 4.82). It was found that abrasive wear rate was higher than W-Cr-Fe nanocomposite coating (0.042 mg/m) despite

its lower sliding wear rate. This is a result of higher porosity of the WC-Cr-Ni coating and the severity of abrasive test. Worn surface was shown in Fig. 4.83.

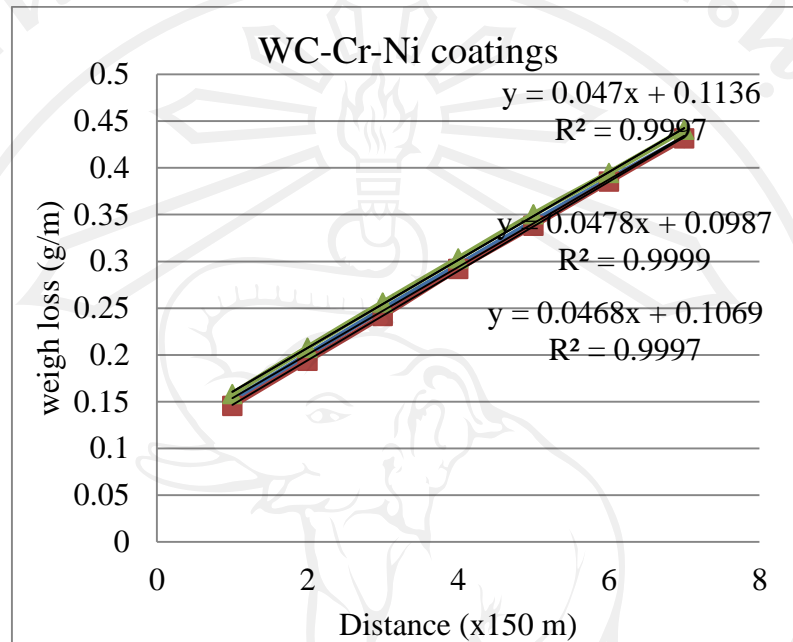


Figure 4.82 Abrasive wear test of WC-Cr-Ni coating.

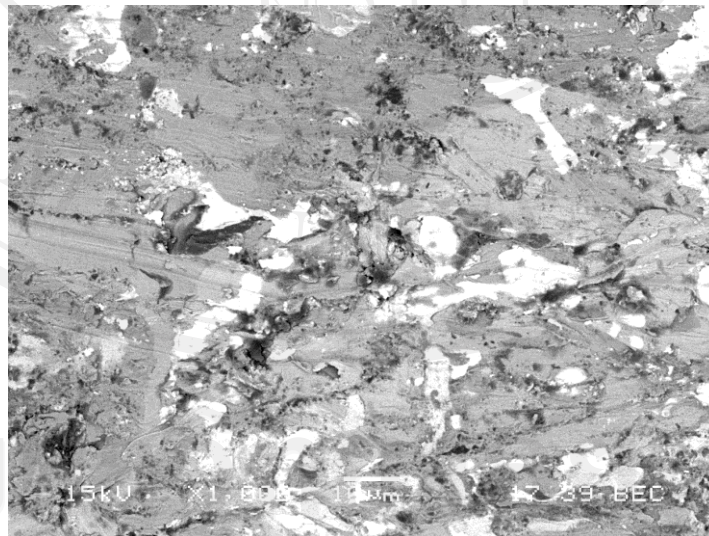


Figure 4.83 SEM micrograph shows worn surface of WC-Cr-Ni coating following abrasive wear test.

4.6.3.3 WC-Cr-Fe coating

Abrasive wear rate of WC-Cr-Fe coating was found to be 0.049 g/m (Fig. 4.84). This coating had the highest wear rate comparison to other coatings which corresponded to its low hardness and high porosity values. SEM image revealed a severe wear track of worn surface as shown in Fig. 4.85.

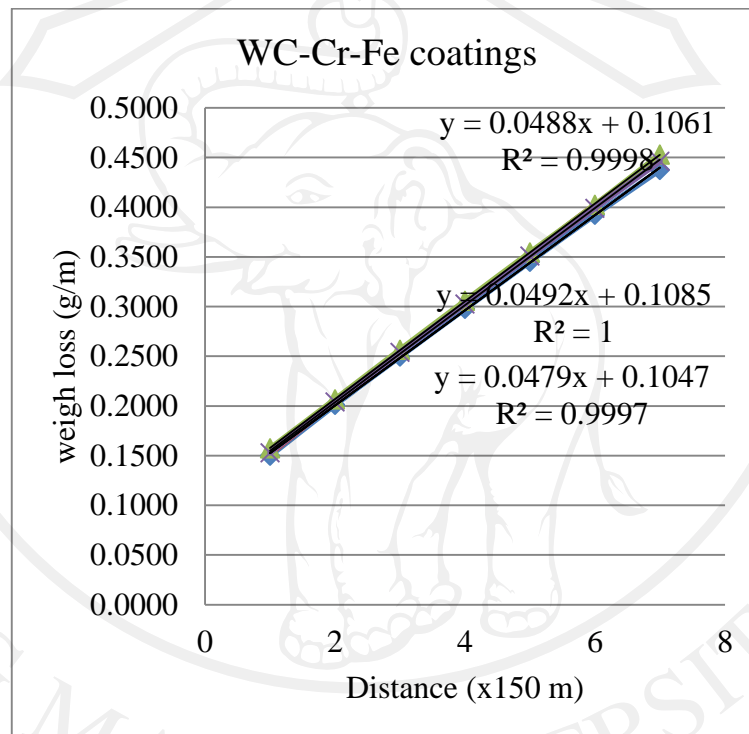


Figure 4.84 Graph showing abrasive wear test of WC-Cr-Fe coating.

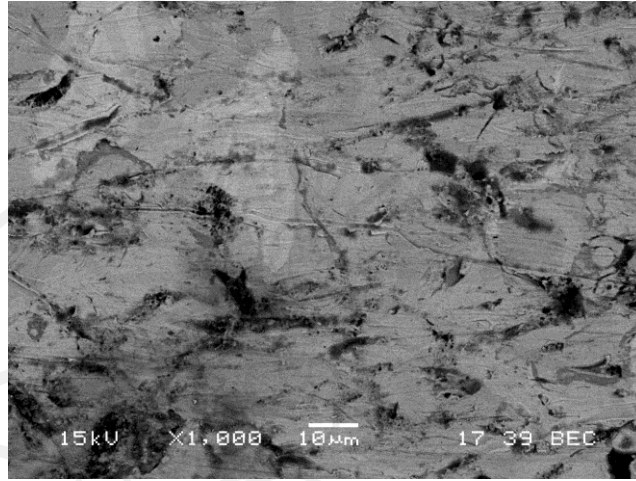


Figure 4.85 SEM micrograph shows worn surface abrasive wear test of WC-Cr-Fe coating.

4.6.3.4 W-Cr-Fe nanocomposite coating

Abrasive wear rate of W-Cr-Fe nanocomposite coating was 0.042 g/m, (Fig. 4.86).

This coating showed the lowest wear rate in a group of arc sprayed coating which corresponded to its high hardness and low porosity. Wear scar of worn surface is also shown in Fig. 87 with rather sever wear.

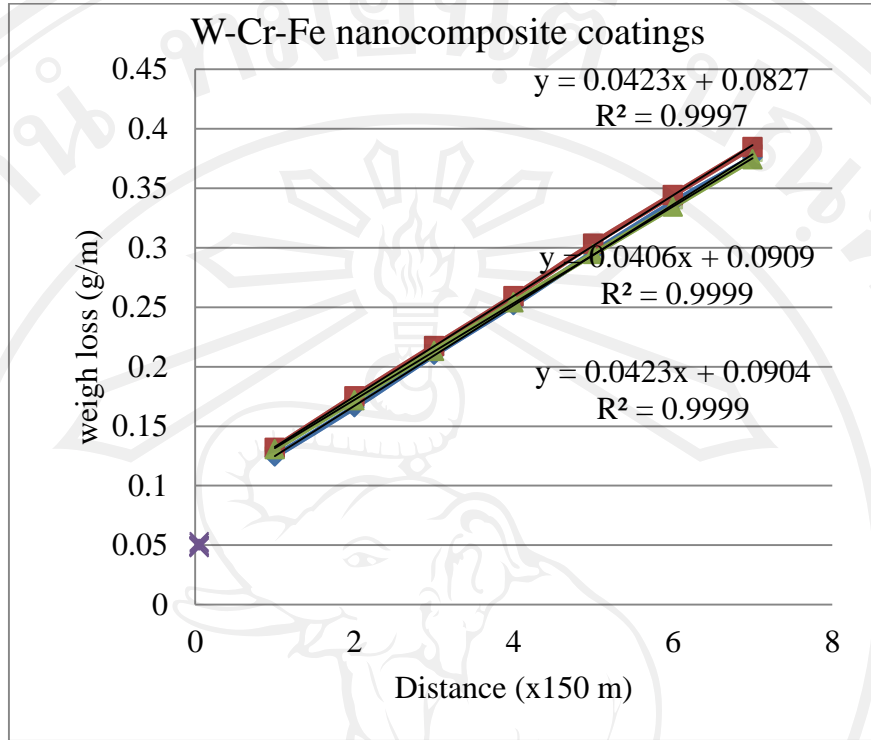


Figure 4.86 Graph showing abrasive wear test of W-Cr-Fe nanocomposite coating.

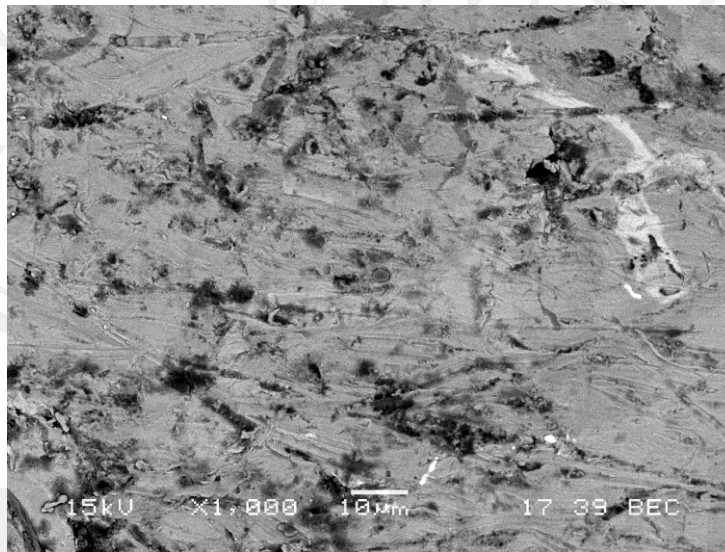


Figure 4.87 SEM micrograph shows worn surface abrasive wear test of W-Cr-Fe nanocomposite coating.

Although the 86WC-4Cr-10Co coating prepared by HVOF showed better coating including characteristics, high hardness, low porosity, dense structure, low surface roughness and high abrasion resistance, coating preparation by HVOF technique is more expensive than arc spray technique. Therefore, this work would emphasis on coatings fabricated by arc spray technique.

4.6.3 Summary of coating wear performance

The sliding wear test by pin on disk technique show that WC-Cr-Ni coating had the lowest of volume loss (0.0334 mm^3) which is two times lower than those of other two core wires coatings. This could be due to a high content of WC. [32,33,35]. The WC-Cr-Fe and W-Cr-Fe nanocomposite coating contain mainly metal alloy structure which is lower sliding wear resistance. Worn surface showed delamellar along with micro-cracking (Fig. 4.88). It is also found that a WC-Cr-Fe coating had the highest volume loss (0.0718 mm^3).

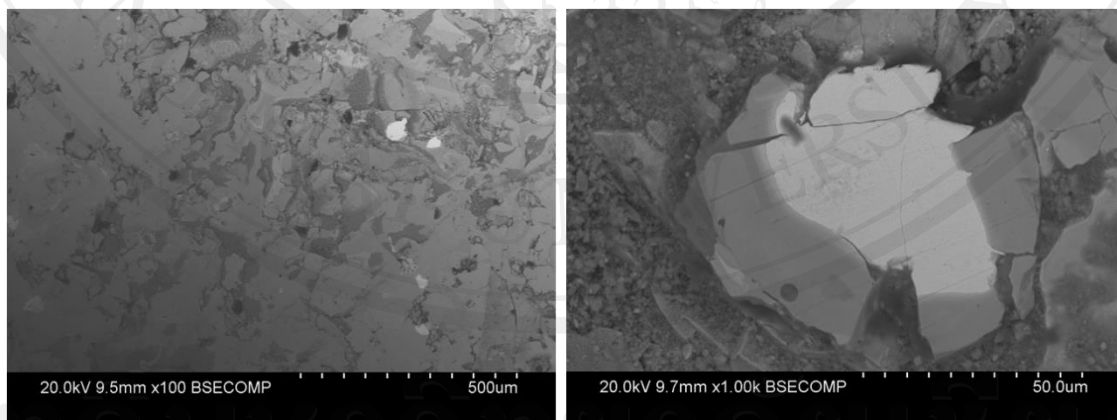


Figure 4.88 SEM micrograph shows low and high magnification of sliding wear scar of coatings.

Abrasive wear rates of cored wire coatings including WC-Cr-Ni, WC-Cr-Fe, and W-Cr-Fe nanocomposite coatings were 0.047, 0.049 and 0.041 mg/m, respectively. It was

found that W-Cr-Fe nanocomposite coating had lower wear rate than other coatings which corresponded to its high hardness and very dense microstructure. WC-Cr-Ni coating had a comparable wear rate with that of WC-Cr-Fe coating. Although WC-Cr-Ni coating had high hardness due to higher tungsten carbide content, it exhibited less dense structure which responsible for lower wear resistance. This influence of microstructure on wear resistance of coating corresponds well with other reports [14-16].

Wear scar of coatings were also investigated as shown in Fig. 4.89. All coatings showed principal cutting mechanism along with plastic deformation and cracking that responsible for coating mass loss. Severe damage of WC-Cr-Ni coating was clearly seen in Fig. 89a. W-Cr-Fe nanocomposite had generally smoother worn surface than others and mainly from plastic deformation.

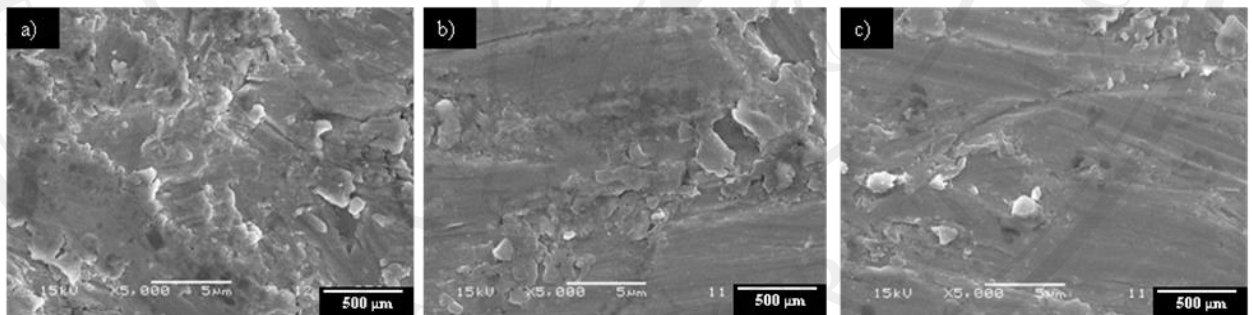


Figure 4.89 SEM micrograph shows abrasive wear scar of coatings: (a) WC-Cr-Ni (b) WC-Cr-Fe and (c) W-Cr-Fe nanocomposite coating.

4.7 Test of plunger coating under simulated conditions

The test of all plunger coatings was operated under simulated conditions by testing rig. Results of the plunger coating test are as follow.

4.7.1 Pump pressure measurement

Testing of all 3 types of plunger coatings under the simulated conditions while setting of specified pressure at 6 bars at 100000m test distance. It was found that in the pipe was nearly constant. As can be seen from Fig 4.90 showing pressure and distance of the plunger during the test.

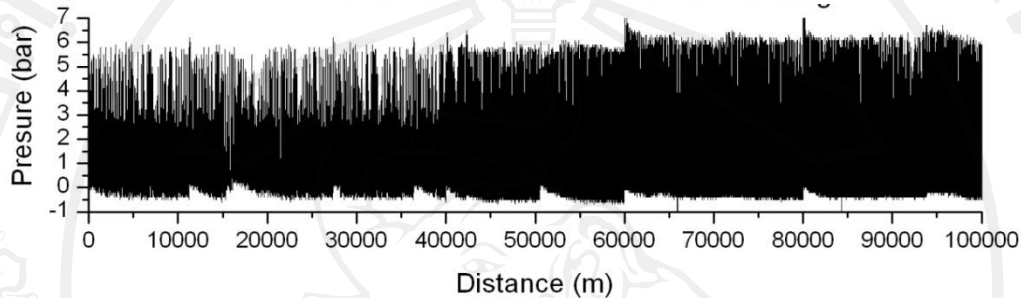


Figure 4.90 Plot of pressure and test distance of plunger coating (WC-Cr-Ni cored wire) tested under simulation conditions.

4.7.2 Characterization of plunger coating worn surface

Characterization of worn surface of plunger coating following the test was carried out by optical microscope. CMM technique for diameter measurement and roughness measurement.

Fig. 4.91 shows the worn surface of the plunger coating. Scratch occurred along the length of all three plunger coatings with some small scratch and large scratch. Roughness measurement of worn surface showed that WC-Cr-Fe nanocomposite coating had the lowest roughness of $0.58\mu\text{m}$. Worn surface of WC-Cr-Fe coating showed the highest roughness of $0.82\mu\text{m}$ corresponded to the highest wear rate as shown in Table 4.26.

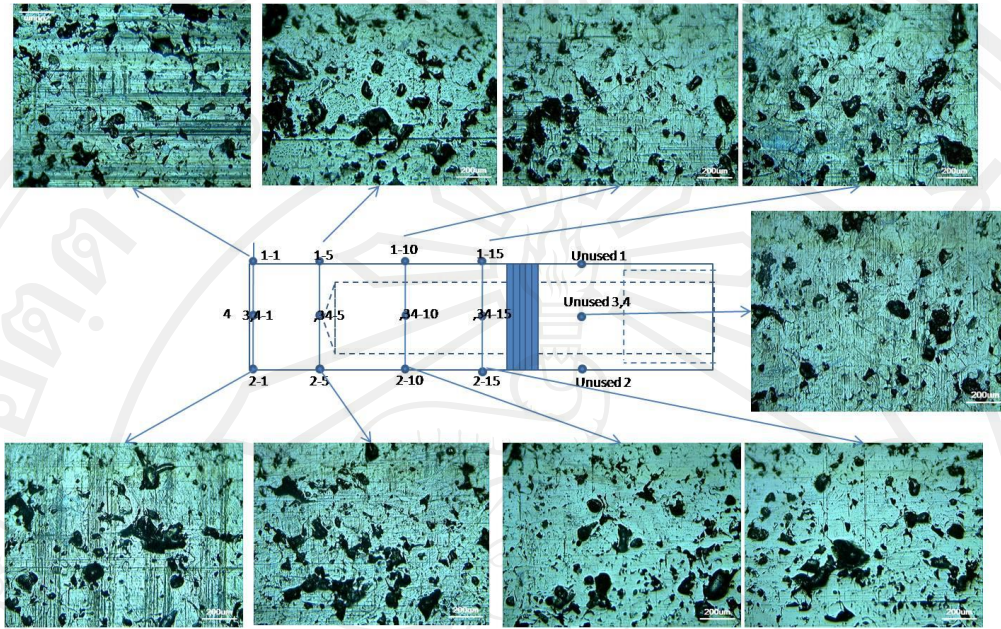


Figure 4.91 OM images shows typical worn surface of the plunger coating (WC-Cr-Ni cored wire) under simulated conditions at 100000m test distance.

WC-Cr-Ni plunger coating showed the lowest in decreasing of diameter which could be due to high WC content in this coatings. However, W-Cr-Fe nanocomposite coating showed a little decrease of diameter as a result of nano-crystal and amorphous structure.

Table 4.26 Characterization of worn surface of plunger coatings.

| Plunger coatings | Roughness (μm) | Diameters decrease (μm) |
|-----------------------|-----------------------------|--------------------------------------|
| WC-Cr-Ni | 0.75 ± 0.1 | *n/a |
| WC-Cr-Fe | 0.82 ± 0.2 | 2.7 ± 0.08 |
| W-Cr-Fe nanocomposite | 0.58 ± 0.1 | 1.1 ± 0.09 |

* lower than detection limit of CMM